PERGAMON

Progress in Biophysics & Molecular Biology 79 (2002) 1–43

Progress in Biophysics & Molecular Biology

www.elsevier.com/locate/pbiomolbio

Review

Observing structure, function and assembly of single proteins by AFM

Daniel J. Müller*, Harald Janovjak, Tiina Lehto, Lars Kuerschner, Kurt Anderson

Max-Planck-Institute of Molecular Cell Biology and Genetics, Pfotenhauer Str. 108, D-01307 Dresden, Germany and BioTEC, Technical University Dresden, D-01062 Dresden, Germany

Abstract

Single molecule experiments provide insight into the individuality of biological macromolecules, their unique function, reaction pathways, trajectories and molecular interactions. The exceptional signal-to-noise ratio of the atomic force microscope allows individual proteins to be imaged under physiologically relevant conditions at a lateral resolution of 0.5–1 nm and a vertical resolution of 0.1–0.2 nm. Recently, it has become possible to observe single molecule events using this technique. This capability is reviewed on various water-soluble and membrane proteins. Examples of the observation of function, variability, and assembly of single proteins are discussed. Statistical analysis is important to extend conclusions derived from single molecule experiments to protein species. Such approaches allow the classification of protein conformations and movements. Recent developments of probe microscopy techniques allow simultaneous measurement of multiple signals on individual macromolecules, and greatly extend the range of experiments possible for probing biological systems at the molecular level. Biologists exploring molecular mechanisms will benefit from a burgeoning of scanning probe microscopes and of their future combination with molecular biological experiments.

Keywords: Single molecule imaging; Single molecule force spectrometry; Conformation

Contents

1. Introduction 3

2. Single protein imaging by AFM 4

3. Characterizing protein structures 6
   3.1. Molecular motors 6
      3.1.1. F-adenosine triphosphate (ATP) synthase rotors 6
      3.1.2. The ϕ29 rotary motor 6

*Corresponding author. Tel.: +49-351-210-2586; fax: +49-351-210-2020.
E-mail address: mueller@mpi-cbg.de (D.J. Müller).

0079-6107/02/$ - see front matter
PII: S0079-6107(02)00009-3

3.2. Ion pumps and channels . . . 7
3.2.1. Bacteriorhodopsin . . . 7
3.2.2. Halorhodopsin . . . 9
3.2.3. Potassium channel . . . 9
3.3. Membrane channels . . . 10
3.3.1. Aquaporin1 (AQP1) . . . 10
3.3.2. Aquaporin Z (AqpZ) . . . 10
3.3.3. Major intrinsic protein (AQP0) . . . 11
3.3.4. Porin outer membrane protein F (OmpF) . . . 12
3.4. Proteins involved into photosynthesis . . . 12
3.4.1. Photosystem I . . . 12
3.4.2. Light-harvesting complex 2 . . . 12
3.5. Toxins . . . 12
3.5.1. Cholera toxin . . . 13
3.5.2. Cry1Aa . . . 13
3.5.3. α-hemolysin . . . 14
3.5.4. VacA . . . 14
3.6. Chaperonins and proteasomes . . . 15
3.6.1. GroE chaperone system . . . 15
3.6.2. 20 S proteasome . . . 16
3.7. Cellulose . . . 16

4. Identifying structural details of proteins . . . 17
4.1. Antibody labeling . . . 17
4.2. Correlation to structural data derived from complementary methods . . . 18
4.3. Identification by replacement of polypeptide loops . . . 19
4.4. Identification by removal of polypeptide loops . . . 20
4.5. Identification by removal of polypeptide ends . . . 20
4.6. When can a polypeptide cleavage be imaged? . . . 20

5. Flexibility and conformational variability of protein surfaces . . . 21
5.1. Flexibility of protein surfaces . . . 21
5.2. Surface structures of proteins can depend on intermolecular interactions . . . 22

6. Observing single protein assemblies . . . 23
6.1. Assembly of proteins attached to a membrane . . . 23
6.2. Assembly of transmembrane proteins . . . 23

7. Observing protein function . . . 25
7.1. Conformational changes of a bacterial surface layer (S-layer) . . . 25
7.2. Channel closure of OmpF porin . . . 26
7.3. Conformational changes of gap junction . . . 27
7.4. Working cycle of a chaperone . . . 28

8. Measuring electrostatic properties . . . 29
8.1. Detecting surface charges of membranes . . . 29
8.2. Detecting the electrostatic potential of a transmembrane channel . . . 30

9. Controlled manipulation of single proteins . . . 30
9.1. Manipulation of individual proteins . . . 31
9.2. Imaging, manipulating and detecting forces of individual proteins . . . 31
9.3. Imaging and unfolding of single proteins . . . 33

10. Perspectives 33
10.1. High-speed AFM 34
10.2. Improved force control 35
10.3. Simultaneous detection of optical signals 36
10.4. Simultaneous detection of multiple parameters 36
10.5. Imaging and nanomanipulation of single proteins 36
References 37

1. Introduction

Biological life may be viewed as a hierarchy of molecular processes, where complexity is further compounded by the fact that individual proteins can have many different functions. Conventional biological techniques, however, only detect sufficient signals from large protein assemblies. Consequently, the measured function of a protein species is commonly enveloped by a Gaussian distribution. But how do proteins behave and function individually? Which reaction pathways do they choose? What are their trajectories and how do they interact with each other? What aspects of their structure give rise to variance in their behavior?

A decade ago the first atomic force microscopy (AFM; Binnig et al., 1986) topographs resolving structural details of native proteins were published (Hoh et al., 1991, 1993). Progress increasing the spatial resolution of protein topographs has been achieved recently in several laboratories by optimizing sample preparation (Czajkowsky et al., 1998a; Mou et al., 1995; Müller et al., 1997a; Scheuring et al., 1999a) and image acquisition (Möller et al., 1999, 1999a; Putman et al., 1992) methods, and by continuous developments of the instrumentation (Han et al., 1996; Hansma et al., 1994a, b; Putman et al., 1994; Tamayo et al., 2000; Viani et al., 1999). Presently topographs of protein surfaces revealing details with a lateral resolution of 0.5 nm and a vertical resolution of 0.1 nm can be recorded routinely (Baker et al., 2000; Fotiadis et al., 2000; Müller and Engel, 1999; Müller et al., 1999a, b; Scheuring et al., 1999b; Seelert et al., 2000). These results, obtained at ambient temperatures and in buffer solution, are prerequisites to observe single biological macromolecules at work (Engel and Müller, 2000) and to study complex pathways of their interactions. In contrast to other microscopic techniques, the outstanding signal-to-noise (S/N) ratio of the AFM topograph allows not only the location of single molecules, but also the observation of their structural details. This creates new experimental possibilities; in particular, it has become possible to study the structural and functional individuality of biological molecules and to investigate factors stimulating their variance. Additionally, observation of biological molecules by AFM does not require them to be labeled or otherwise specially treated. Thus in principle, every single component of a macromolecular assembly can be observed in an AFM topograph, opening new avenues to study pathways of molecular biological reactions.

We will begin by reviewing the work from contributors in the field, in which single biomolecules were imaged at submolecular resolution. After this, we report examples where structural details of protein have been explicitly identified, examples observing the dynamic behavior and the variability of protein structures and of their assembly, examples observing the protein function, and examples detecting multiple biochemical parameters of a protein simultaneously.

2. Single protein imaging by AFM

In contrast to conventional imaging instruments such as light and electron microscopes the AFM uses a stylus to raster-scan a surface, thereby monitoring the height profile of the sample. The stylus is mounted on a cantilever, whose deflection is detected with piconewton ($pN = 10^{-12}$ N) sensitivity. A feedback loop controls the spatial movement of a piezoelectric positioner with sub-Angstrom (10^{-10} m) accuracy and, thereby, the tracking of the biological sample by the AFM stylus. Such accuracy is required to achieve high-resolution topographs and to control the interaction between the stylus and the biological object. It is important to ensure that the forces interacting locally between the tip of the AFM stylus and the biological sample do not exceed several 10 pN, because higher forces would lead to sample distortion or even disruption. Polypeptide loops of aquaporin (AQP), bacteriorhodopsin, gap junction and ϕ29 connector undergo reversible structural changes by interaction forces between 50 and 150 pN (Müller et al., 1995, 1997b, 2001b; Scheuring et al., 1999b). These values correlate well with biomolecular forces lying between a few pN, as generated, e.g., by Kinesin and myosin (Howard, 2001), and $\approx$300 pN, as required to mechanically unfold a protein (Fisher et al., 1999; Oesterhelt et al., 2000; Rief et al., 1997). The forces applied to the biological sample can be minimized by selecting the appropriate AFM imaging mode (Han et al., 1996; Hansma et al., 1994a; Humphris et al., 2001; Putman et al., 1994; Tamayo et al., 2000; Viani et al., 1999), by electrostatic balancing (Müller et al., 1999a) and by optimizing the AFM feedback-loop parameters (Möller et al., 1999).

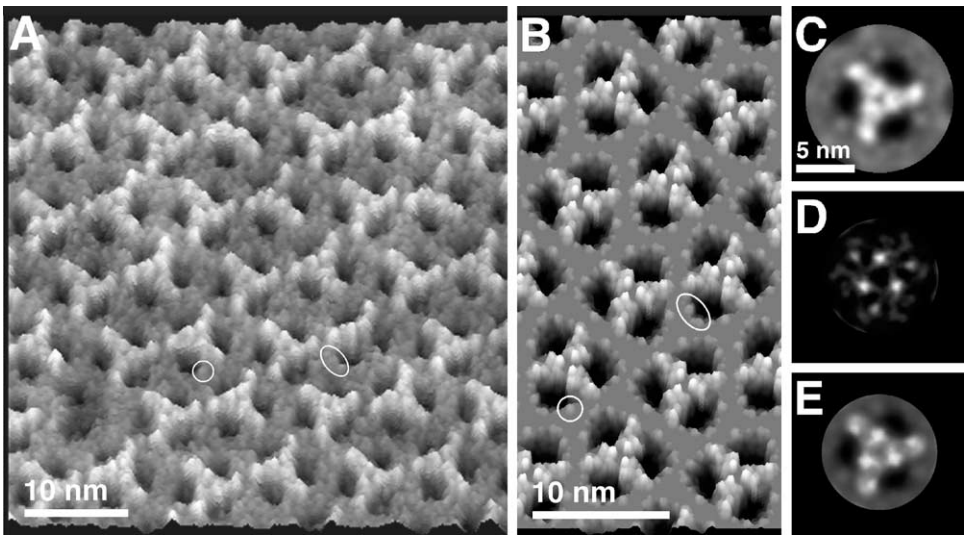

Fig. 1. OmpF porin imaged in buffer solution using AFM. (A) AFM topograph as revealed in 300 mM KCl, 10 mM Tris–HCl, pH 7.8. Single porin trimers assembled into rectangular unit cells of the 2D crystal are clearly visible. The ellipse indicates short β-strand-connecting turns observed on individual porin monomers (comp. Fig. 2). (B) Periplasmic surface of the atomic OmpF porin model rendered at 0.3 nm resolution. The OmpF trimers were embedded in a membrane (gray smooth surface) and arranged according to the rectangular lattice ($a = 7.6$ nm; $b = 13.5$ nm) of the 2D OmpF crystals investigated experimentally. The topographs A and B are displayed as relief tilted by 5°. (C) Three-fold symmetrized correlation averaged porin trimer ($n = 247$) generated from (A). (D) The SD map of (C) had a vertical range from 0.05 to 0.23 nm. (E) To assess variable structural regions, the average and SD map were superimposed.

Fig. 1 compares a high-resolution AFM topograph of native OmpF porin from *Escherichia coli* (Fig. 1A) with its atomic model derived from X-ray crystallography (Fig. 1B). It is clearly visible, that the excellent S/N ratio of the AFM topograph allows characteristic substructures of single proteins to be resolved. In contrast, the atomic model of porin represents an averaged result, based on diffraction on many proteins. However, careful observation indicates structural deviations between individual proteins and the atom model. These deviations are expressed in the average (Fig. 1C) and standard deviation (SD) map (Fig. 1D) of all proteins imaged in the topograph. Whereas the averaged topograph highlights common structural details of the protein majority, the SD map indicates regions exhibiting structural variability. This structural variability can be directly compared with the temperature coding of the protein structure derived by other structural methods such as nuclear magnetic resonance (NMR), X-ray and electron crystallography, which is a measure for structurally less defined regions (Müller et al., 1999b; Philippsen et al., 2002). A stereo presentation of the averaged topography, the SD map and the atomic OmpF porin structure presents all these information within one figure (Fig. 2). A remarkable correlation among AFM topography, SD, the atomic structure and temperature factors are observed, although the experimental conditions used to determine both structures were different. Whereas OmpF porin observed using AFM was embedded in a lipid bilayer exposed to buffer solution and room temperature, the OmpF porin investigated by X-ray crystallography was solubilized in detergent and crystallized in three dimensions.

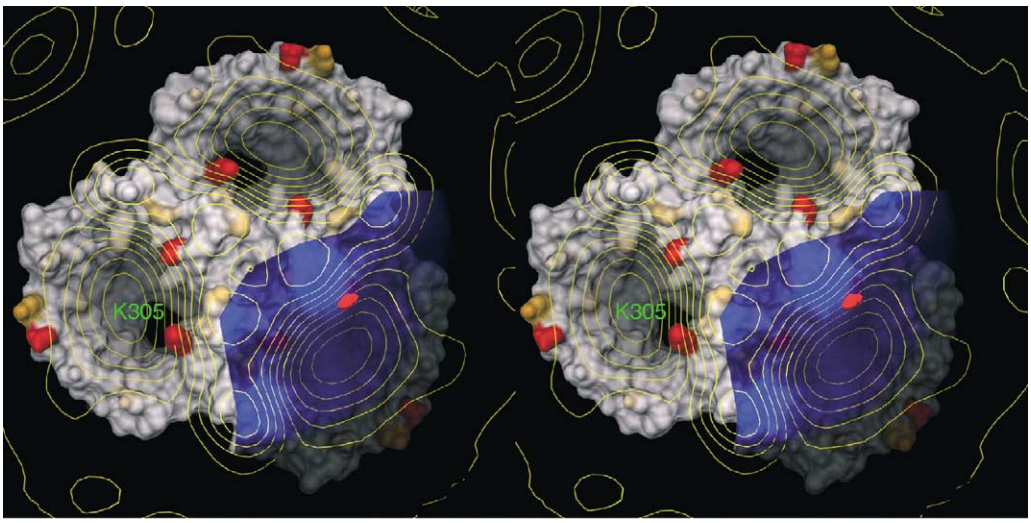

Fig. 2. Comparison of surface topography and atomic model of OmpF porin using stereo presentation. The AFM surface (yellow contour plot) represents the correlation average calculated from the topograph recorded in Fig. 1. The underlying molecular surface derived from the crystal structure is color coded according to crystallographic temperature factors: white below 60, white to yellow from 60 to 70, yellow to red from 70 to 80 and red above 80. The three undefined (red) sidechains are K10, E183 and K305, of which only K305 is not consistent with the AFM topograph since it protrudes through the topograph and, therefore, directly interacts with the AFM probe. Superimposed onto the lower right pore is the SD map of the correlation average (Fig. 1C), with bright blue indicating region of height variability.

3. Characterizing protein structures

To observe proteins at work they should preferably reside in their native environment. For soluble proteins this is a physiological buffer, while membrane proteins additionally require being embedded in a lipid bilayer. Here we present an overview of water-soluble and membrane proteins that have been investigated at submolecular resolution using AFM.

3.1. Molecular motors

3.1.1. F-adenosine triphosphate (ATP) synthase rotors

F_0F_1-adenosine triphosphate (ATP) synthases use the energy of a transmembrane proton (or Na^+) gradient to synthesize the biological energy currency ATP. The cation flow appears to drive the transmembrane rotor of the integral membrane complex F_0, which is coupled to a molecular shaft (Engelbrecht and Junge, 1997; Stock et al., 2000; Wilkens and Capaldi, 1998) that activates the catalytic F_1 complex. In current models of the F_0F_1-ATP synthases, the number of subunits forming the ion driven rotor has direct implications for the $H^+(Na^+)$/ATP stoichiometry and for the molecular mechanism of ATP synthesis. Until recently, it was postulated that this rotor comprises 12 subunits. This conclusion was mainly based on cross-linking experiments, genetic engineering (Jones and Fillingame, 1998), model building (Groth and Walker, 1997; Rastogi and Girvin, 1999) and biochemical data that suggest that four protons are required for the synthesis of one ATP. Furthermore, it was assumed that this stoichiometry would be constant regardless of the biological species from which the ATP synthases originates.

To prove this structural model AFM has been exploited to image isolated ion driven rotors from chloroplast (Seelert et al., 2000) and bacterial (Stahlberg et al., 2001) ATP synthase. In both investigations, the number of subunits per rotor could be directly counted in the unprocessed AFM topograph (Fig. 3). Surprisingly, it was found that the rotor from ATP synthase of *Ilyobacter tartaricus* consisted of 11 subunits (Fig. 3A), while that from spinach chloroplast ATP synthase exhibited 14 subunits (Fig. 3B). Additionally, the X-ray analyses of yeast F_0F_1-ATP synthase yielded a decameric rotor (Stock et al., 1999). AFM imaging of rotors from chloroplast ATP synthase purified by three independent procedures revealed that the rotor stoichiometry remained unaffected by the purification method (Seelert et al., in preparation). Complementary analysis of single defective bacterial and chloroplast rotors showed their circular diameter to be independent of the number of subunits missing. This led to the conclusion that the subunits themselves determine the rotor diameter and, thereby constrain how many subunits would fit into the rotor (Müller et al., 2001a). The occurrence of different stoichiometries among biological species is not yet understood (Ferguson, 2000).

3.1.2. The ϕ29 rotary motor

The head to tail connector of the *Bacillus subtilis* bacteriophage ϕ29 represents a rotary motor that hydrolyzes ATP to power pack double-stranded DNA into a precursor capsid. In contrast to the rotary motor of ATP synthase, the ϕ29 connector converts a mechanical rotation to a translational movement of DNA. In the bacteriophage the DNA, connector and prohead form a complex of concentric structures with 10-, 12- and 5-fold symmetry, respectively (Simpson et al., 2000). These constitute a movable central spindle, intervening ball race, and a static outer

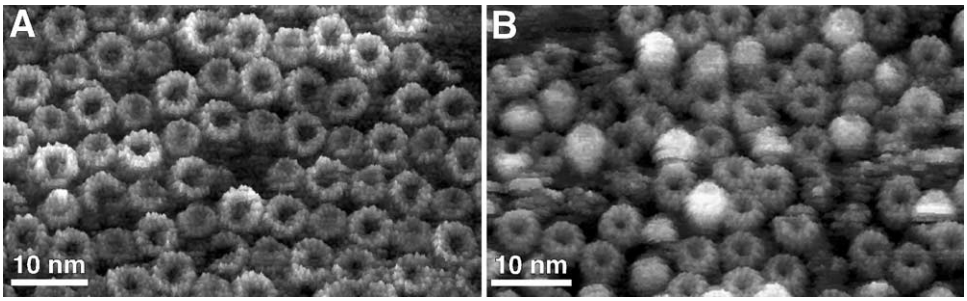

Fig. 3. Cation driven rotors of F_0F_1-ATP synthases. The individual subunits of the cylindrical rotors represent two transmembrane α-helices connected by a polypeptide loop. (A) The sodium driven rotor of the F_0F_1-ATP synthase from *I. tartaricus* exhibits 11 subunits. (B) The proton driven rotor of the F_0F_1-ATP synthase from spinach chloroplast is formed by 14 subunits. The topographs were recorded using contact mode AFM, exhibit vertical full gray levels of 2 nm and were obtained in 300 mM KCl, 10 mM Tris–HCl, pH 7.8 (A) and 25 mM $MgCl_2$, 10 mM Tris–HCl, pH 7.8 (B).

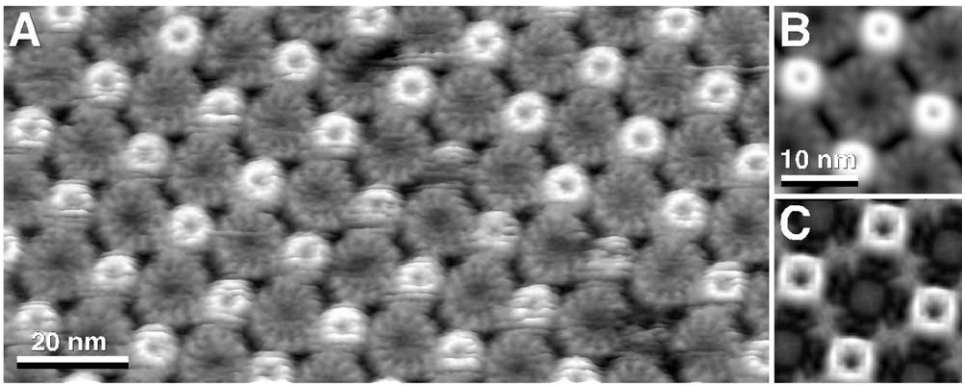

Fig. 4. Rotary rotors of ϕ29 bacteriophages imaged by contact mode AFM. (A) Raw data obtained in 500 mM KCl, pH 7.8, 10 mM Tris–HCl. The 2D crystal exhibited a p4212 symmetry with each thick end of the connector surrounded by four thin ends of adjacent connectors. (B) Four-fold symmetrized correlation average of (A). (C) SD map of the correlation average. Full gray level ranges: 4 nm (A), 3 nm (B), and 0.5 nm (C). All images are displayed as surface relief tilted by 5°.

assembly (stator), which powers the motor. The ϕ29 connector symmetry is of importance in understanding the energetic mechanism of DNA translocation. AFM topographs of native connectors assembled into a two-dimensional (2D) lattice clearly show substructures of the connector ends (Fig. 4). The 12 subunits of the wide connector end can be directly revealed from the unprocessed data (Müller et al., 1997b).

3.2. Ion pumps and channels

3.2.1. Bacteriorhodopsin

The light driven proton pump bacteriorhodopsin converts the energy of "green" light (500–650 nm) into an electrochemical proton gradient, which in turn is used for ATP production by ATP synthases. Bacteriorhodopsin represents one of the most extensively studied membrane

proteins (Haupts et al., 1999; Oesterhelt, 1998). Its structural analysis has revealed the photoactive retinal embedded in seven closely packed α-helices (Essen et al., 1998; Grigorieff et al., 1996; Kimura et al., 1997; Luecke et al., 1998; Pebay-Peyroula et al., 1997), which builds a common structural motif among a large class of related G-protein coupled receptors (Baldwin, 1993; Hargrave, 1991; Helmreich and Hofmann, 1996; Henderson et al., 1990). Together with adjacent lipids bacteriorhodopsin molecules assemble into trimers, which are packed into 2D hexagonal lattices, the purple membrane of *Halobacterium salinarum*.

A high-resolution topograph of the extracellular purple membrane surface (Fig. 5A) revealed the arrangement of tripartite protrusions on a trigonal lattice ($a = b = 6.2 \pm 0.2$ nm). The protrusions exhibited a maximum height difference to the lipid membrane of 0.53 ± 0.07 nm. The power spectrum (Fig. 5B) of the topography extended to the 11th order indicating a lateral resolution of 0.49 nm (Müller et al., 1999b). Distinct features on the extracellular surface can be assigned to individual polypeptide loops exposed to the aqueous solution (Fig. 5C). The most prominent protrusion of bacteriorhodopsin is the β-hairpin in the loop connecting the transmembrane α-helices B and C. Because parts of the loop dip into the lipid bilayer (Heymann et al., 1999) not all features of the loop were visualized by AFM. This demonstrates one limitation of AFM imaging as a surface sensitive technique. As a result of this loop conformation, the major protrusion of this loop was observed to be located between helices C and G and not between helices B and C. While the shoulder close to helix A represents the N-terminus, loop FG exhibits an enhanced SD (Fig. 5D) indicating an increased structural variability and alternative conformations which are not reflected in the atomic models derived from electron and X-ray crystallography (Heymann et al., 1999).

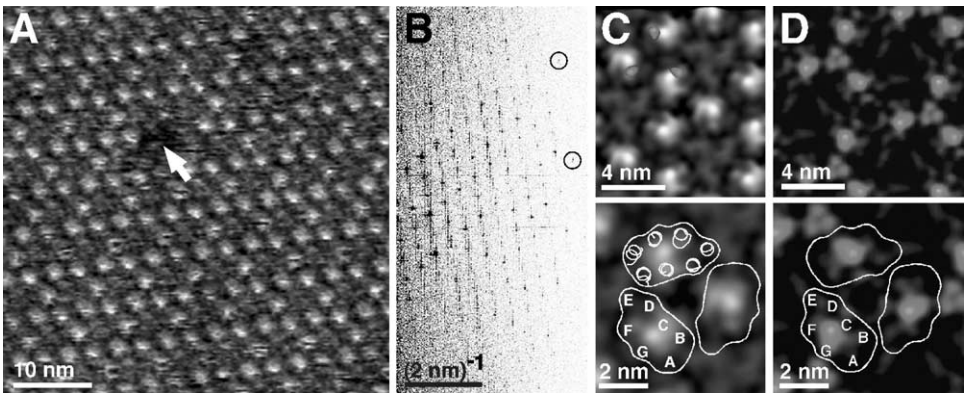

Fig. 5. Extracellular purple membrane surface recorded in buffer solution (A). The purple membrane surface exhibits a defect having the size of a bacteriorhodopsin trimer (→). (B) The power spectrum of (A) extends to the 11th order indicating a lateral resolution of 0.49 nm. (C) Averaged extracellular surface of the bacteriorhodopsin trimer (average of 320 unit cells). The correlation average is displayed in perspective view (top, shaded in yellow brown) and in top view (bottom, in blue) with a vertical brightness range of 1 nm. To assess the flexibility of the different structures, SD maps were calculated (D) and had a range from 0.07 (lipid) to 0.12 nm (region of the FG loop). Surface regions exhibiting a SD above 0.1 nm are superimposed in red-to-white shades on the top of figure (C). The topograph was recorded in buffer solution (100 mM KCl, 10 mM Tris–HCl, pH 7.8) at a loading force of 100 pN. The outlined bacteriorhodopsin trimer representing sections close to the extracellular surface of the lipid membrane was obtained after merging five atomic models of bacteriorhodopsin derived from electron and X-ray crystallography (Heymann et al., 1999).

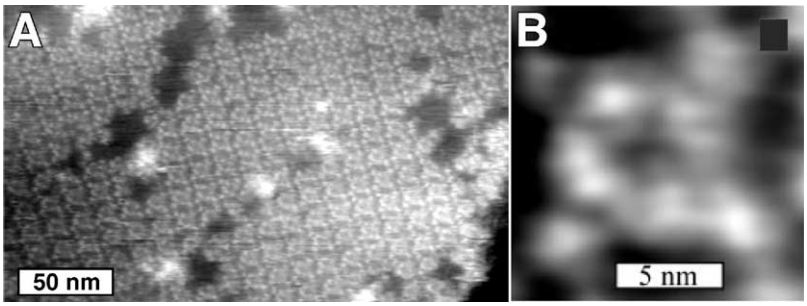

Fig. 6. Reconstituted halorhodopsin tetramers recorded in buffer solution (A). Tetramers are arranged in an upside down orientation: each tetramer is surrounded by four tetramers oriented with their opposite surfaces towards the membrane surface. The membrane surface exhibits several defects having the size of one to several halorhodopsin molecules. (B) Average of the unit cells showing the tetramer in more detail. This topograph was recorded using contact mode AFM and in 150 mM KCl, 10 mM Tris–HCl, pH 8 (Image courtesy of M. Fritz, Goettingen).

3.2.2. Halorhodopsin

H. salinarum thrives in high-temperature saturated salt brines that are exposed to bright sunlight. Coexisting beside bacteriorhodopsin, halorhodopsin exploits light of a similar spectral range to maintain the iso-osmolarity of the cytoplasm by transporting chloride ions into the cell (Bamberg et al., 1993). In contrast to bacteriorhodopsin, halorhodopsin is not assembled into crystalline patches and, therefore, must be crystallized for analysis by diffraction methods (Kunji et al., 2000). The recently published atomic structure revealed high structural similarities between bacteriorhodopsin and halorhodopsin (Kolbe et al., 2000).

AFM topographs revealed from reconstituted halorhodopsin (Fig. 6) showed neighbored tetramers to be orientated with their extracellular and cytoplasmic surface towards the membrane surface (Persike et al., 2001). Each halorhodopsin molecule was resolved by a single protrusion and the correlation with the structural model of halorhodopsin (Kolbe et al., 2000) suggested this protrusion to present the largest polypeptide loop connecting two transmembrane α-helices.

3.2.3. Potassium channel

Potassium (K^+) channels have many functions; they stabilize membrane potential, set the resting potential, keep fast action potentials short, terminate periods of intense activity, time the interspike intervals during repetitive firing, and generally lower the effectiveness of excitatory inputs on a cell when they are open (Hille, 1992). Most K^+-channels are formed by four symmetrically arranged subunits, each exhibiting six putative transmembrane segments. The P-domains (polypeptide loops) connecting transmembrane segments were thought to fold into the channel and to be responsible for its selectivity. Voltage gated Shaker type K^+-channels, however, are composed of at least two types of subunits: the pore-forming Kvα subunits, and the cytoplasmic Kvβ subunits, which modulate the gating behavior of the pore. To see whether the water-soluble Kvβ2 subunits, belonging to the class of Kvβ subunits, form supramolecular structures, they were expressed and purified without the Kvα subunits, then imaged by AFM (Fig. 7; van Huizen et al., 1999). The AFM topographs showed single tetramers formed by the Kvβ2 subunits. This finding suggests that the binding of the Kvβ tetramer to the K^+-channel

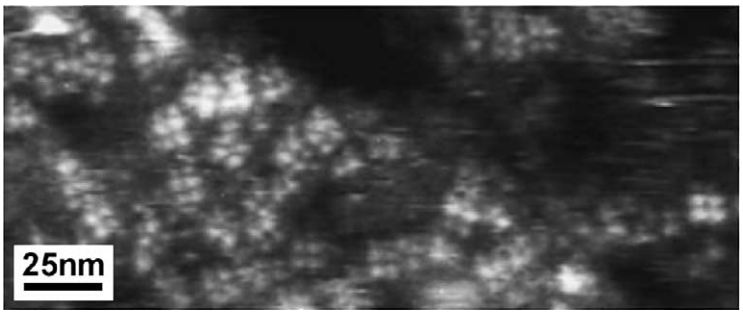

Fig. 7. Purified hydrophilic K$v\beta$2 subunits from a K^+-channel expressed in Sf9 insect cells. This topograph reveals square shaped complexes suggesting that single K$v\beta$2 subunits assemble into tetramers. Each domain of a tetramer exhibits a diameter of $\approx$4.1 nm and is separated by $\approx$6 nm from the adjacent domain. The height of individual complexes corresponds to $\approx$5.1 nm. The topograph was recorded in 150 mM NaCl, 10 mM Tris–HCl, pH 7.2 using contact mode AFM (Image courtesy of D. Czajkowsky and Z. Shao, Charlottesville).

covers its entire cytoplasmic surface. Therefore, it can be excluded that direct interactions between the N-terminal surface of the K$v\alpha$ tetramer and other soluble proteins occur after binding of the K$v\beta$ tetramer.

3.3. Membrane channels

3.3.1. Aquaporin1 (AQP1)

AQPs represent a family of channel proteins transporting water and, in some cases, certain neutral metabolites across biological membranes. Many among them regulate the hydraulic conductivity of membranes in which they reside, allowing rapid water permeation. AQPs are highly selective, and can transport up to a billion water molecules per second, depending on the osmotic gradient imposed (Agre et al., 1993; Pohl et al., 2001; Saparov et al., 2001). Sequence analysis and the available three-dimensional (3D) structures suggest a common architecture for the AQP family—AQP shape tetramers of which each monomer is formed by six transmembrane α-helices surrounding two inward pointing loops. The diversity of AQP isoforms, however, challenges the understanding of how these membrane channels are modified obtaining their specific functional variations (Heymann and Engel, 1999, 2000).

Aquaporin 1 (AQP1) functions as a highly specific and constitutively active water conducting pore in human erythrocyte membranes (Agre et al., 1993; Saparov et al., 2001). AQP1 tetramers reconstituted in lipid membranes readily crystallize and alternately expose their intracellular and extracellular surface (Hasler et al., 1998a). To generate high-resolution topographs, AQP1 was deglycosylated with endoglycosidase F/N-glycosidase F (Walz et al., 1996). After this treatment both surfaces of the AQP1 tetramer were observed at subnanometer resolution, revealing the structural details of polypeptides connecting transmembrane helices.

3.3.2. Aquaporin Z (AqpZ)

Aquaporin Z (AqpZ) of *E. coli* is responsible for the maintenance of cell turgor during the volume expansion of cell division (Borgnia et al., 1999; Calamita et al., 1998). Reconstituted into a

membrane bilayer AqpZ readily assembled into a 2D crystal. Individual AqpZ tetramers of these crystals expose either their extracellular or cytoplasmic surface (Scheuring et al., 1999b). Although the projection maps derived from cryo-electron microscopy (Scheuring et al., 1999b; Walz et al., 1995) and the sequence homology of AQP1 and AqpZ show high similarities, their surface structures appear to exhibit significant differences (Heymann and Engel, 1999, 2000). This variation of the surface structures may not necessarily play a role in the function of AQP1 and AqpZ. However, it may be of relevance for those AQPs which were thought to gate by structural changes of their polypeptide loops or ends.

3.3.3. Major intrinsic protein (AQP0)

The major intrinsic protein (MIP or AQP0) expressed in eye lens fiber cells is the founding member of the AQP family (Gorin et al., 1984). Tetrameric AQP0 extracted and purified from sheep lens fiber cells was reconstituted in the presence of lipids to assemble highly ordered tetragonal 2D arrays (Hasler et al., 1998b). AFM investigations of these samples showed that AQP0 forms double layered crystals, with the intracellular surfaces facing out of the double layer and the extracellular surfaces of both layers facing toward each other (Fotiadis et al., 2000). Nanodissection of the upper membrane layer exposed the extracellular surface of the underlying protein layer (Fig. 8A). The high-resolution topograph provides insight into the arrangement of the extracellular AQP0 surfaces. The model of the extracellular surfaces derived from the AFM data shows the two adjacent layers interacting with each other through a 'tongue-and-groove' fit (Fig. 8B). This finding supports a role for AQP0 not only as water channel (Varadaraj et al., 1999) but also as a mediator of adhesion between adjacent cells.

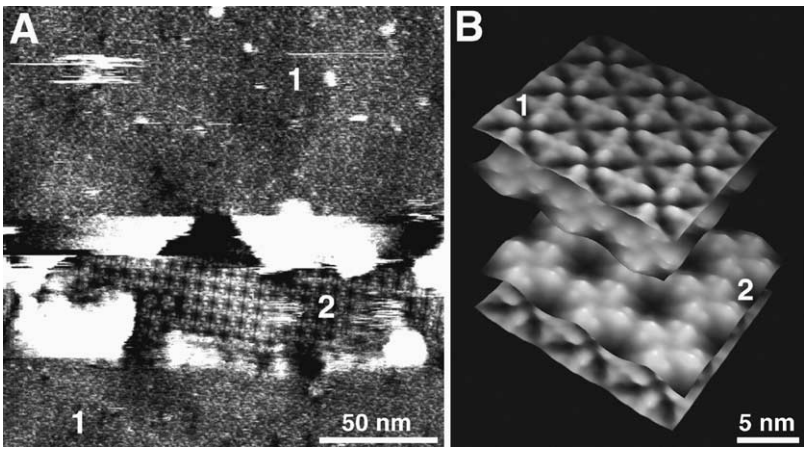

Fig. 8. Nanodissection and intermembraneous interaction of AQP0. Major intrinsic proteins (AQP0) from lens fiber cells form highly ordered tetragonal, double-layered arrays by reconstitution into the lipid bilayer. (A) Both AQP0 surfaces are visible after the partial removal of the upper layer by the AFM probe (2). Careful analysis of such topographs allows the simultaneous observation of submolecular resolution of the cytoplasmic (1) and extracellular (2) AQP0 surfaces. The contact mode topograph was recorded in buffer solution (150 mM KCl, 50 mM $MgCl_2$, 10 mM Tris–HCl, pH 8.8). (B) Computer reconstruction of a double-layered AQP0 crystal showing the interaction of the extracellular surfaces and the co-registration of the two crystalline sheets. The cytoplasmic surface of AQP0 (1) is characterized by a weak corrugation compared to the extracellular one (2). The topographs exhibit vertical brightness ranges of 1.8 nm (A) and 1.4 nm (B) (Image courtesy of D. Fotiadis, Basel).

3.3.4. Porin outer membrane protein F (OmpF)

The transmembrane channel forming outer membrane protein F (OmpF) porin establishes stable trimeric structures in the outer membrane of *E. coli*. The 340 amino acids (aa) long polypeptide of the OmpF monomer is folded into 16 antiparallel β-strands shaping a large hollow β-barrel structure perforating the membrane (Cowan et al., 1992). An infolding loop forms the eyelet of each barrel constricting the passage of ions and of hydrophilic solutes up to an exclusion size of ≈ 600 kDa (Nikaido and Saier, 1992; Schirmer, 1998). In contrast to the short polypeptide loops connecting β-strands on the periplasmic surface (Figs. 1 and 2) loops at the extracellular surface are much longer (Fig. 21) protruding 13 ± 2 Å from the lipid surface. Image averaging enhanced the porin trimer structure but blurred the substructure of the three domains surrounding a central vestibule, indicating that the loops forming the protrusions were rather flexible. This structural flexibility is essential for the OmpF function and allows conformational changes associated with the gating conditions of the transmembrane pore (see Section 7).

3.4. Proteins involved into photosynthesis

3.4.1. Photosystem I

Photosystem I (PSI) and photosystem II (PSII) are pigment-containing reaction centers of oxygenic photosynthesis in cyanobacteria and plants. Each of the two reaction centers consists of many subunits, some of which are extrinsically bound to the transmembrane parts of the complex. To gain insight into how these extrinsic proteins are arranged on the membrane surface of PSI Fotiadis et al. used electron and AFM. After identifying the lumenal and stromal surfaces of the PSI complex it was possible to locate all three extrinsic subunits PsaC, -D and -E (Fotiadis et al., 1998). By using the AFM stylus as a 'nanotweezer' it was possible to remove individual extrinsic proteins and to image the interfaces between the subunits and the stromal surface of the PSI core (see Section 9.1).

3.4.2. Light-harvesting complex 2

After absorbing light the light-harvesting complex 2 (LHC2) transfers excitation energy to the light-harvesting complex 1 (LHC1). In a further step, LHC1 transforms this energy to the reaction center, which establishes an electrochemical energy across the membrane. In agreement with previously published electron microscopy data, the AFM topographs of reconstituted LHC2 from *Rubrivivax gelatinosus* revealed nine identical subunits forming a transmembrane cylindrical structure (Scheuring et al., 2001). After enzymatic removal of the C-terminal region the height of the LHC2 cylinders was significantly reduced. Because of this large structural change it was suggested that the C-terminal end is located at the membrane exterior, thereby partly forming a α-helical structure.

3.5. Toxins

A key issue of toxicology, which has been investigated using the AFM, is how toxins associate with membranes. Cholera toxin was among the first proteins to be imaged at high resolution with the AFM (Mou et al., 1995; Yang et al., 1993). These results were achieved by Z. Shao and coworkers through the introduction of innovative preparation techniques for covering a

supporting surface by model lipid membranes and to simultaneously maintain the membrane ability to associate with toxins.

3.5.1. Cholera toxin

Cholera toxin produced by *Vibrio cholerae* binds to ganglioside GM1 receptors. Through an unknown mechanism, this causes the enzymatic subunit to be clipped from the rest of the protein and transferred into the cell. Once inside the cell the subunit causes an increase in cellular cyclic adenosine monophosphate (cAMP), leading to an overactivity of luminal sodium pumps. The electrolytes in the gut cause water to leave the cells, resulting in the characteristic diarrhea. Mimicking the physiological relevant lipid and GM1 composition of the membrane Shao and coworkers used AFM to observe the insertion of cholera toxin (Mou et al., 1995; Yang et al., 1993). It was found that cholera toxin inserted in fluid-phase bilayers containing 10 mol% GM1 at room temperature (Fig. 9). Single monomers and the central channel of the cholera toxin B-pentamer (Merritt et al., 1998) were clearly resolved in the topograph.

3.5.2. Cry1Aa

Cry1Aa from *B. thuringienesis* forms toxic pores in larval midgut epithelial cell membranes of insects. Although the crystal structure of solubilized Cry1Aa has been solved, the question of how Cry1Aa inserts and assembles in the host membrane remains to be answered. Using Fourier transform infrared spectroscopy (FTIR) and AFM, the group of Grimellec demonstrated that Cry1Aa inserts spontaneously into lipid bilayers (Vie et al., 2001). This process is associated with large conformational changes of Cry1Aa. Topographs of toxins inserted into lipid bilayers show Cry1Aa to form tetrameric structures with a central depression of 1.5 nm in diameter.

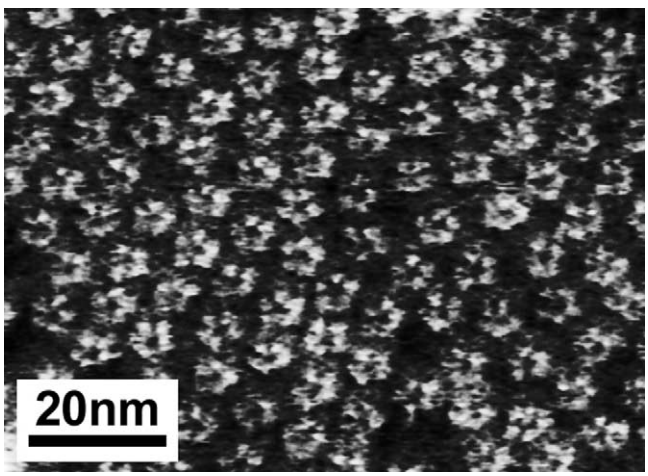

Fig. 9. Cholera toxin B-oligomer from *V.cholerae* associated with ganglioside GM1 receptors embedded in a DPPC bilayer. Both the 5 subunits and the central pore are observed in most of the oligomers. The topograph was recorded in 10 mM Tris, 20 mM NaCl, at pH 7.5 and exhibits a vertical range of ≈ 1 nm (Image courtesy of D. Czajkowsky and Z. Shao, Charlottesville).

3.5.3. α-hemolysin

Hemolysins are bacterial toxins that assemble from a water-soluble, monomeric species to form membrane-bound oligomer on the surface of target cells. They create water-filled channels that lead to cell death and lysis through the leakage of small molecules and ions through the large (water-filled) central channel. Recent structural analysis using X-ray crystallography suggested α-hemolysin monomers from *Staphylococcus aureus* assemble into a heptamer with each monomer exhibiting 16 antiparallel β-strands and four short α-helices (Song et al., 1996). It was suggested that the mushroom shaped heptamer penetrates the membrane bilayer at its stem, with the cap extending into the extracellular space.

Shao and coworkers used AFM to image the association of α-hemolysin with the membrane bilayer (Czajkowsky et al., 1998b). Surprisingly, they found that hemolysin forms hexameric pores in the membrane bilayer (Fig. 10), in apparent contrast to the initial view of α-hemolysin heptamer formation (Song et al., 1996). However, these results may indicate a polymorphism of the subunit stoichiometry of the α-hemolysin oligomer. The molecular mechanism driving the variable oligomeric formations is currently not understood and it is expected that the study of such mechanisms will provide valuable insights into the poorly understood process of membrane protein assembly.

3.5.4. VacA

The toxin VacA, secreted by *Heliobacter pylori* inserts into cell membranes and induces vacuolation of acidic intracellular components, causing chronic superficial gastritis in humans.

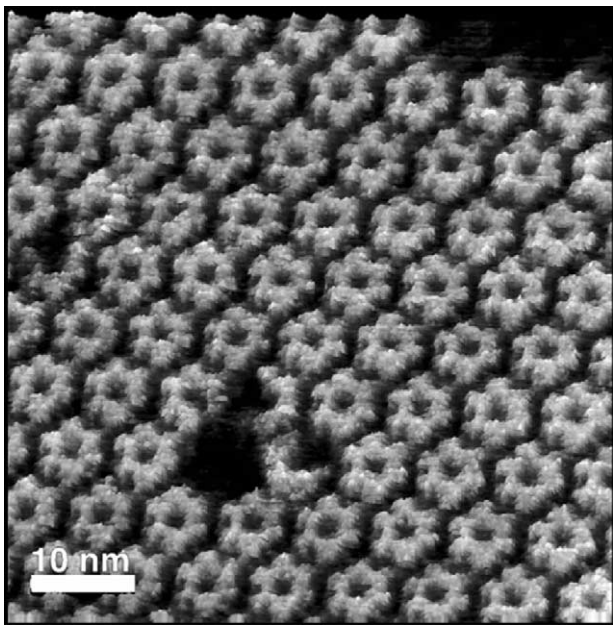

Fig. 10. α-Hemolysin from *S. aureus* associated with a lipid membrane. The topograph clearly shows that α-hemolysin forms hexamers. Experiments using two different lipid mixtures (total lipid extract from bovine heart and a mixture of eggPC and dioleoylphosphatidylcholine/dioleoylphosphatidylserine (1:1)) did not influence the stoichiometry of the hemolysin oligomer. The topography was recorded in 10 mM sodium phosphate at pH 7.2, exhibits a vertical range of 1 nm, and is displayed as relief tilted by 5° (Image courtesy of D. Czajkowsky and Z. Shao, Charlottesville).

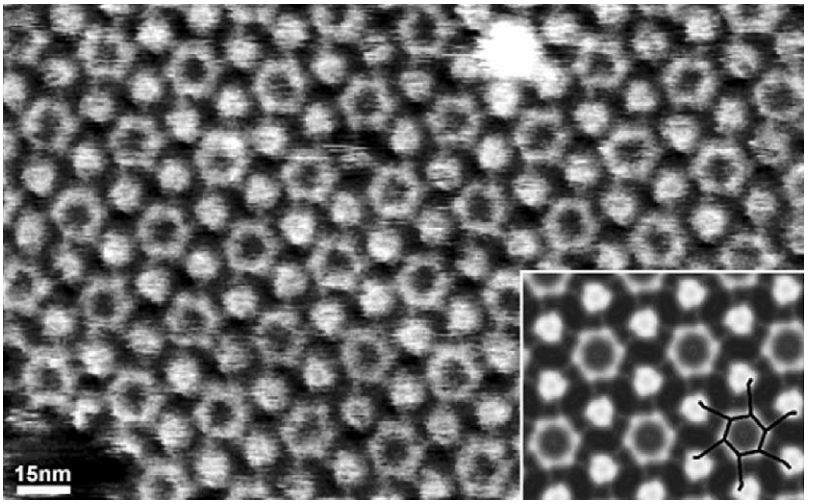

Fig. 11. Vacuolating (VacA) toxin from *H. pylori* inserted into a lipid bilayer. Individual hexameric pores assembled into a hexameric assembly are separated by 22 nm. Inset, the correlation average enhances the structural details observed. Single subunits of neighbored pores are connected by peripheral domains (inset, schematic drawing). The topography of the chemically fixed sample (1% glutaraldehyde) was recorded in 1 mM Hepes, 100 mM $MgCl_2$, pH 7.5 and exhibits a vertical range of 3 nm (Image courtesy of D. Czajkowsky and Z. Shao, Charlottesville).

Investigation of the interaction of VacA with model lipid membranes under a variety of conditions using AFM suggests that water-soluble VacA dodecamers disassemble at low pH and reassemble into membrane spanning hexamers (Fig. 11; Czajkowsky et al., 1999). Electrophysiological measurements mimicking the AFM experiments show the inserted VacA hexamers to form transmembrane pores (Iwamoto et al., 1999). These data support a model in which VacA is acidified by the low pH of the stomach and interacts directly with the lipid components of the plasma membrane of the gastric epithelium.

3.6. Chaperonins and proteasomes

3.6.1. GroE chaperone system

The GroE chaperone machinery consists of two ring-shaped oligomeric components, GroEL and GroES, which mediate the folding of a large number of proteins in vivo and in vitro. Three different activities have been attributed to the GroE system: (1) preventing aggregation of unfolded polypeptides, (2) allowing polypeptides to fold in a protected environment of the central cavity of GroE and (3) unfolding of kinetically trapped intermediates (Fedorov and Baldwin, 1997; Lilie and Buchner, 1995). AFM images of GroEL (Fig. 12A) and of GroES (Fig. 12B) reported by the group of Shao exhibited a spatial resolution that allowed their seven-fold symmetry to be resolved (Mou et al., 1996a, 1996b). These results, obtained on glutaraldehyde fixed samples, suggested the possibility of obtaining similarly high resolution on the functionally intact GroE machinery (Cheung et al., 2000; Viani et al., 2000; Vinckier et al., 1998). It is thought that the AFM could provide an excellent method to investigate intermediate steps of the complex

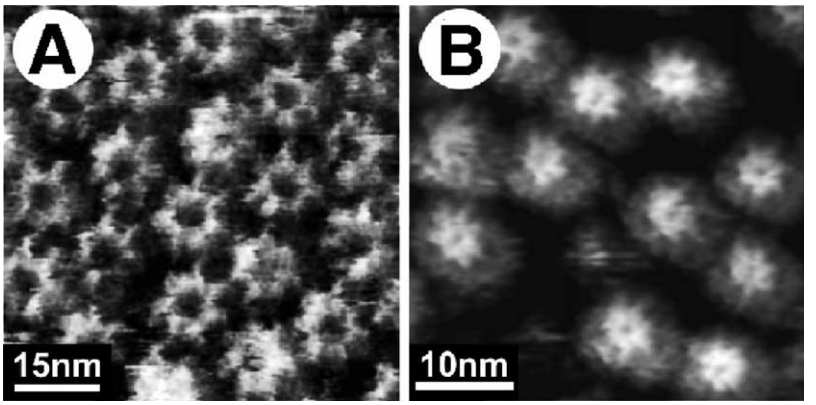

Fig. 12. GroE chaperones. (A) GroEL adsorbed onto mica. The heptameric structures of the cylinders are clearly resolved. (B) GroES adsorbed onto mica. Topographs of the chemically fixed samples (1% glutaraldehyde) were recorded in 1 mM Hepes, 100 mM $MgCl_2$, pH 7.5 and exhibit a vertical range of $\approx$15 nm (A) and of $\approx$3 nm (B) (Image courtesy of Z. Shao, Charlottesville).

formation of GroEL with GroES and of the functional GroE cycle in the presence of substrate (see Section 7.4).

Fig. 12A shows the heptameric symmetry of the apical domains of chaperonin GroEL. After imaging of the apical domains the chaperonins were dissected using the AFM tip as a nanotweezer and the equatorial domains of the lower GroEL half became visible (Mou et al., 1996a, 1996b). Intact GroEL molecules had a channel opening of $\approx$4.3 nm. Although much smaller than GroEL, individual GroES heptamers could also be very well resolved and were found to exhibit a central depression with a diameter of 1.1 nm (Fig. 12B). All images revealed the seven-fold symmetry of the underlying molecular machinery at a lateral resolution of 1–2 nm.

3.6.2. 20 S proteasome

The 20 S proteasome of *Thermoplasma acidophilum* is a macromolecular protease complex that degrades misfolded or regulatory proteins (Baumeister et al., 1998). Composed of 28 subunits, the proteasome exhibits four stacked heptameric rings forming a barrel-shaped structure penetrated by a narrow channel where the proteolytically active sites are located. Dorn et al. (1999) attached histidine-tagged 20 S proteasomes to chelator lipids that were incorporated into membranes supported by mica. AFM topographs showed these proteasomes to be oriented in a well-defined manner. Subsequent analysis of this sample by surface plasmon resonance (SPR) allowed real-time detection of substrate–proteasom complex formation, and of substrate recognition and degradation (Dorn et al., 1999).

3.7. Cellulose

Cellulose is an unbranched polymer of glucose residues joined by β-[1,4] linkages allowing cellulose to form long straight chains. These chains are optimized for the construction of fibers exhibiting a high tensile strength. Two phases I_α and I_β coexist within native cellulose. Whereas

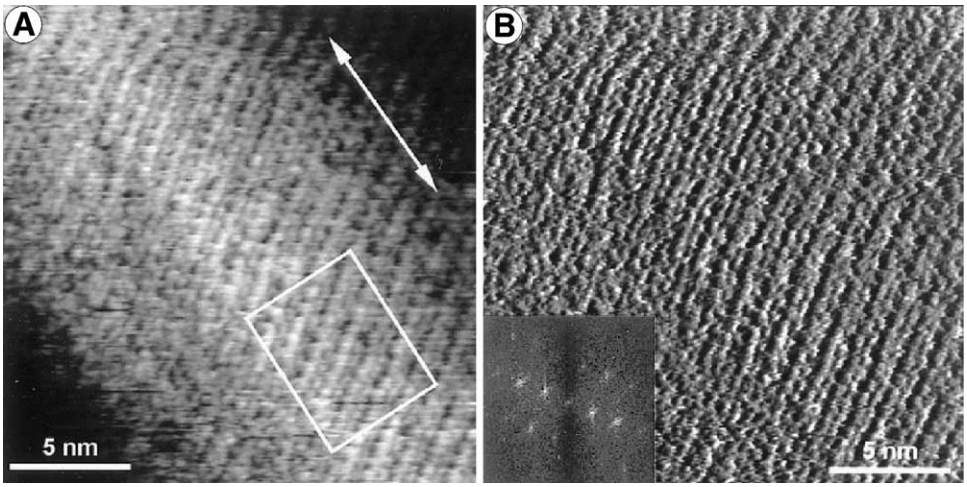

Fig. 13. Cellulose crystal of *Valonia*. Simultaneously recorded topography (A) and error signal (B). The orientation of the cellulose chains is indicated by an arrow. The error signal emphasizes the high-resolution features on the surface. Inset, the fast Fourier transform shows the distinguishing triclinic signature of the surface observed in diffractograms. Images were recorded in water (Image courtesy of M. Miles, Bristol).

their biological origin is not sufficiently explained yet their coexistence and the transformation from one phase into the other remains to be investigated. To reveal insight into this question, AFM was applied to investigate the structural phases of crystalline cellulose from the green alga *Valonia ventricosa* (Baker et al., 1997; Baker et al., 2000). The AFM topographs show the cellulose to exist in microscrystals separated by disordered surface regions. A long-range order of the cellulose surface could not be observed. Fig. 13 shows AFM images acquired from a *Valonia* microcrystal. The unprocessed image allows to observe the spacing of the triclinic planes to be observed at a lateral resolution $<0.5\,\text{nm}$.

4. Identifying structural details of proteins

Although AFM allows to image substructures of single proteins at extremely high-resolution, additional information is often required to confirm the identification or orientation of macromolecules, their surfaces, and subdomains. By definition, antibodies specifically recognize their antigen, and thus can be used to identify proteins, viruses, tissues, cell surfaces and other macromolecular structures. Since antibodies are rather large, they may not be useful for identifying structural details of single proteins. Additionally, antibodies directed against the structure of interest are not always available. Hence, we present an overview of methods suitable to the identification of proteins and their structural details.

4.1. Antibody labeling

To identify the native bacteriorhodopsin surfaces, purple membrane was adsorbed from buffer solution onto a freshly cleaved mica surface. After being rinsed with the same buffer solution, the

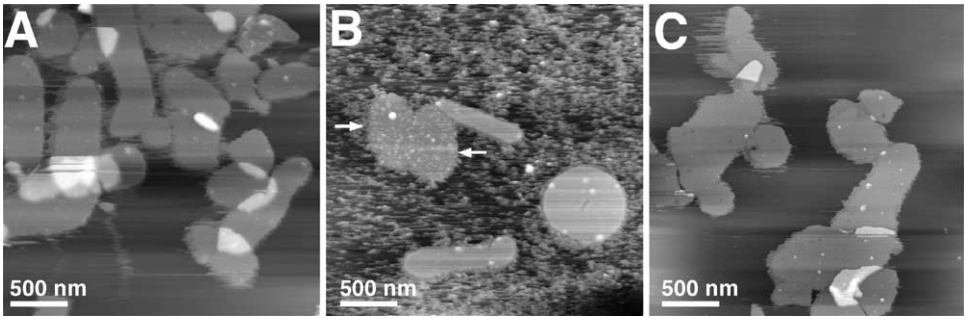

Fig. 14. Immuno AFM of purple membrane. (A) Native purple membrane adsorbed flat on freshly cleaved mica. (B) Antibodies were added to the buffer solution after adsorption of the native membranes yielding some densely labeled membranes (→), while others remained unlabeled. The antibodies were directed against the C-terminus of bacteriorhodopsin located on the cytoplasmic purple membrane surface. Thus, the labeled membranes exposed their cytoplasmic surface towards the aqueous solution. (C) AFM topograph of papain digested purple membrane leading to the removal of the C-terminus. After incubation with antibodies, digested purple membrane remained untextured even after extending the reaction time for antibody binding from 1 to 24 h at room temperature. Imaging buffer: 150 mM KCl, 10 mM Tris, pH 8. The vertical gray level of all topographs correspond to 20 nm.

purple membrane patches were routinely observed in the fluid cell of the AFM (Fig. 14A). At low magnification, no topographic differences between individual membranes were detected. To distinguish between the two surfaces of purple membrane, antibodies directed against the bacteriorhodopsin C-terminus, which is located on the cytoplasmic bacteriorhodopsin surface, were injected into the buffer solution (Müller et al., 1996b). After addition of antibodies some of the labeled membranes exhibited a rough surface (Fig. 14B), whereas others remained as smooth as the membranes shown in Fig. 14A. To further establish the specificity of antibody labeling, the C-terminus was removed by papain digestion of purple membrane. Papain digested purple membrane exhibited the same dimensions and smooth surface texture as native purple membrane. Consistent with the absence of antibody binding in dot immunobinding assays no decoration of the digested membranes was observed (Fig. 14C), even after extending the incubation time with the antibodies from 1 to 24 h (Müller et al., 1996b). These results indicated that purple membranes have been specifically labeled by antibodies directed to the C-terminus when their extracellular surface was in contact with the mica. Thus the smooth patches of purple membrane not labeled by the antibody were oriented with their extracellular surface towards the AFM tip.

4.2. Correlation to structural data derived from complementary methods

As observed in the AFM topograph, the periplasmic surface of the OmpF porin trimer (Fig. 1A; outlined circle) is compromised of tripartite protrusions and three transmembrane channels that are separated by 1.2 nm thick walls. The transmembrane channel has a characteristic elliptical cross section of $a = 3.4$ nm and $b = 2.0$ nm. The arrows point out individual polypeptide loops of a few aa size each connecting two antiparallel β-strands lining the transmembrane pore. Most features recorded in this AFM topograph were correlated directly with the atomic model of the OmpF (Cowan et al., 1992) surface rendered at 0.3 nm resolution (Fig. 1B). Correlation

averaging of the porin trimer enhanced common structural details among individual trimers (Fig. 1C) but blurred variable areas of the subdomains (compare to porin trimers shown in raw data, Fig. 1A). However, the characteristic shape of the transmembrane channel was more pronounced showing an elliptical cross section of $a = 3.4$ nm and $b = 2.0$ nm. Structural features of the periplasmic OmpF trimer exhibiting high variability are represented in the SD map of the average (Fig. 1D). Enhanced values of the SD map are directly correlated to surface structures expected to have enhanced flexibility (Fig. 1B).

4.3. Identification by replacement of polypeptide loops

The replacement of a polypeptide loop results in a structural change of the membrane protein surface that may be directly observed by AFM. Eight polypeptide residues of the EF loop of bacteriorhodopsin were replaced with 24 residues from the third cytoplasmic loop of bovine rhodopsin. The third cytoplasmic loop of rhodopsin is important in signal transduction from the retinal in rhodopsin to its G-protein, transducin (Helmreich and Hofmann, 1996) and interacts with rhodopsin kinase, which phosphorylates light-activated rhodopsin, and with arrestin, which displaces transducin from light-activated, phosphorylated rhodopsin. To directly observe this substituted loop, purple membrane containing the mutant bacteriorhodopsin was imaged by AFM under physiological conditions to a resolution of 0.7 nm (Fig. 15A; Heymann et al., 2000). The major difference in the topographs between the cytoplasmic surfaces of the mutant (Fig. 15A)

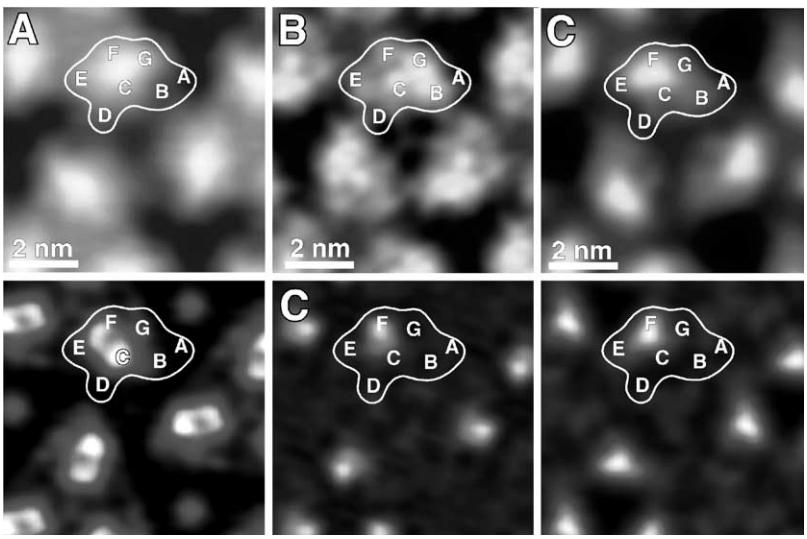

Fig. 15. Polypeptide loop replacement and removal induces structural changes of the protein surface. Three-fold symmetrized correlation average of the cytoplasmic mutant IIIN (A), of wild type (C) purple membranes and of purple membrane after proteolytic removal of the EF loop (B). The lower images represent the SD map of the averages. AFM topographs, from which the averages were calculated, were recorded at minimal applied forces to ensure that the flexible EF loops were observed in their native, unperturbed conformation. The vertical gray levels of the maps correspond to 2 nm (A), 0.5 nm (A, bottom), 1 nm (B), 0.2 nm (B, bottom), 1.2 nm (C) and 0.2 nm (C, bottom). The outlined bacteriorhodopsin shape and the position of the α-helical ends (named A–G) facing the cytoplasmic surfaces were derived from atomic models (Heymann et al., 2000).

and wild type purple membrane (Fig. 15C) is the much larger EF loop projecting towards the C-terminus.

4.4. Identification by removal of polypeptide loops

AFM studies have repeatedly shown, that it is possible to directly image individual polypeptide loops of proteins. These loops can be removed enzymatically to identify structural features of membrane protein surfaces. Digestion of the third rhodopsin loop from mutated bacteriorhodopsin (Fig. 15B) with V8-protease did not affect the purple membrane crystallinity but changed the appearance of its cytoplasmic surface. The AFM topograph showed a significant reduction in the major protrusion of bacteriorhodopsin compared to the undigested surface of the purple membrane mutant (Fig. 15B) and the ends of helices E and F became clearly visible (Heymann et al., 2000). Interestingly, AFM topographs of wild type (Fig. 15C) and of mutated (Figs. 15A and B) purple membrane did not show any indication of the largest polypeptide chain located at the cytoplasmic surface, the C-terminus (24 aa). The simplest interpretation is that this residue is too unstructured to allow imaging (see also next section).

4.5. Identification by removal of polypeptide ends

This alternative method to identify the surfaces of membrane proteins is illustrated by the selective cleavage of terminal polypeptide sequences of major intrinsic protein (AQP0) from sheep lenses (Fotiadis et al., 2000) and of AqpZ from *E. coli* (Scheuring et al., 1999b). Topology predictions and antibody labeling of AQP0 place the approximately 5 kDa C-terminal region on the cytoplasmic surface of the lens fiber cell membrane. The native cytoplasmic surface of AQP0 tetramers, reconstituted into a bilayer and assembled into a 2D crystal, exhibited maximum globular protrusions of 0.8 ± 0.1 nm. After removal of the C-terminal tail with carboxypeptidase Y the cytoplasmic surface appeared coarser, and the averaged structure revealed the partial loss of four prominent protrusions leaving a central cavity within the AQP0 tetramer (Fotiadis et al., 2000). Similar experiments were performed on AqpZ. AqpZ has an N-terminal fragment of 26 aa located on the cytoplasmic surface. After enzymatic removal of the N-terminal fragment, the altered substructures observed by AFM allowed identification of the cytoplasmic surface of AqpZ (Scheuring et al., 1999b). It is important to note, that neither the extracellular surface of AQP0 nor of AqpZ appeared to be structurally affected by the enzymatic digestion of polypeptides located at the cytoplasmic surface.

4.6. When can a polypeptide cleavage be imaged?

From above AFM measurements it follows, that the conformation of the AqpZ N-terminal fragment (26 aa) was too flexible to be imaged with subnanometer resolution (blurred protrusion), but was structurally sufficiently stable to distort the scanning stylus, thereby preventing the visualization of other substructures on the cytoplasmic surface. The C-terminal fragment of AQP0 existed in a structurally more stable conformation and could, therefore, be imaged at high resolution. In contrast, the C-terminal region of bacteriorhodopsin, consisting of 25 aa, is not observed and apparently does not influence the visualization of surrounding substructures by

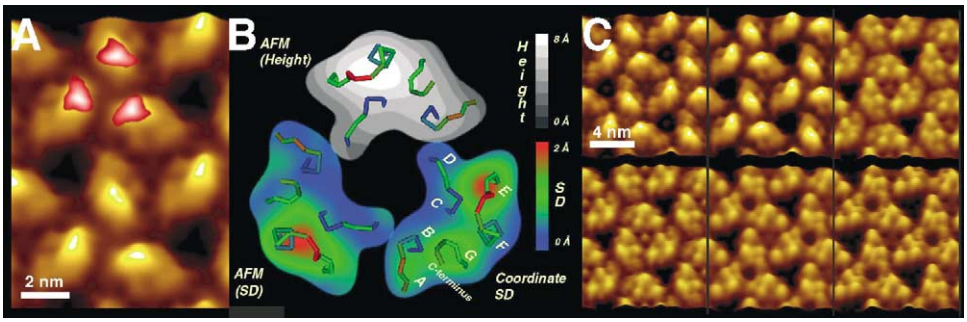

Fig. 16. Quantitative analysis of the native cytoplasmic purple membrane surface. (A) Correlation average of the AFM topograph recorded at an applied force of 100 pN (Müller et al., 1999b). Regions with enhanced flexibility are derived from SD maps and superimposed in red to white shades. (B) Different surface properties of bacteriorhodopsin. The surface loops are shown as backbone tracings colored according to the backbone coordinate root-mean-square deviation (SD) calculated after merging five different atomic models of bacteriorhodopsin (Heymann et al., 1999). The gray scale image shows the height map determined by AFM (A) with the prominent protrusion representing the EF loop. The colored monomers represent the SD between the atomic models, and of the height measured by AFM. (C) Unraveling the force induced structural changes of the cytoplasmic surface by multivariate statistical analysis. Top left: purple membrane imaged at 80 pN. Top center: same membrane imaged at approximately 100 pN. Top right: at about 150 pN the EF loop is bent away while the shorter polypeptide loops of the cytoplasmic surface become visible. Bottom row: three conformations differing in their central protrusion are observed at approximately 180 pN. Topographs exhibit a vertical range of 1 nm and are displayed as relief tilted by 5°.

AFM (compare to Fig. 16). These results illustrate, that polypeptide ends of proteins exhibit individual conformations and stabilities. While the conformation of the C-terminal region of AQP0 is stable enough to be reproducibly imaged at subnanometer resolution, the N-terminal region of AqpZ is structurally less stable than the C-terminal end of AQP0 but more stable than the disordered C-terminal domain of bacteriorhodopsin (Belrhali et al., 1999; Essen et al., 1998; Grigorieff et al., 1996; Heymann et al., 1999; Luecke et al., 1999; Mitsuoka et al., 1999) which is not detected by AFM (Müller et al., 1999b). Accordingly, a structural change caused by the cleavage of a polypeptide can only be observed by the AFM if the polypeptide was reproducibly detected before its removal.

5. Flexibility and conformational variability of protein surfaces

5.1. Flexibility of protein surfaces

The cytoplasmic surface of purple membrane can undergo distinct structural changes when imaged by AFM. At a force of 100 pN applied to the AFM cantilever the bacteriorhodopsin surface is imaged in an unperturbed conformation (Müller et al., 1999b) correlating excellently to its atomic model (Heymann et al., 1999) (Figs. 16A and B). The highest protrusion of the cytoplasmic surface represents the polypeptide loop connecting transmembrane α-helices E and F. This structural element exhibits an intrinsic flexibility (Fig. 16B) allowing helix F to undergo enhanced conformational changes during the proton pumping mechanism (Pfeiffer et al., 1999).

At slightly higher applied forces of 150 pN the EF loop is bent away by the AFM tip, and shorter loops connecting α-helices A and B, C and D, and the C-terminal region of bacteriorhodopsin become visible (Fig. 16C). This structural change is reversible. Besides demonstrating the capability of the AFM to image membrane proteins at subnanometer resolution, these results point out the sensitivity of this technique allowing the native conformation of single polypeptide loops to be imaged and manipulated in a controlled manner.

Similarly, the force induced modulation of flexible protein substructures was observed on the ϕ29 phase connector (Müller et al., 1997b) and on AqpZ from *E. coli* (Scheuring et al., 1999b). Interestingly, the observed EF loop flexibility is of importance for the efficiency with which bacteriorhodopsin transports protons across the bacterial membrane (Pfeiffer et al., 1999). The flexibility of the thin end of the DNA transporting ϕ29 connector (Fig. 4) is also of fundamental functional importance (Simpson et al., 2000). The localized structural flexibility observed on AqpZ (Fig. 8), however, may suggest novel aspects to the functional properties of this water channeling protein. One may speculate whether the observed flexible AqpZ structures might also change their conformation according to osmotic pressure, and whether such structural changes influence the water transporting mechanism of the channel.

5.2. Surface structures of proteins can depend on intermolecular interactions

The function and properties of proteins depend on their cellular environment and the macromolecular complex within which they function. Since the structure and function of a protein are closely related, it remains important to study parameters which influence the protein structure.

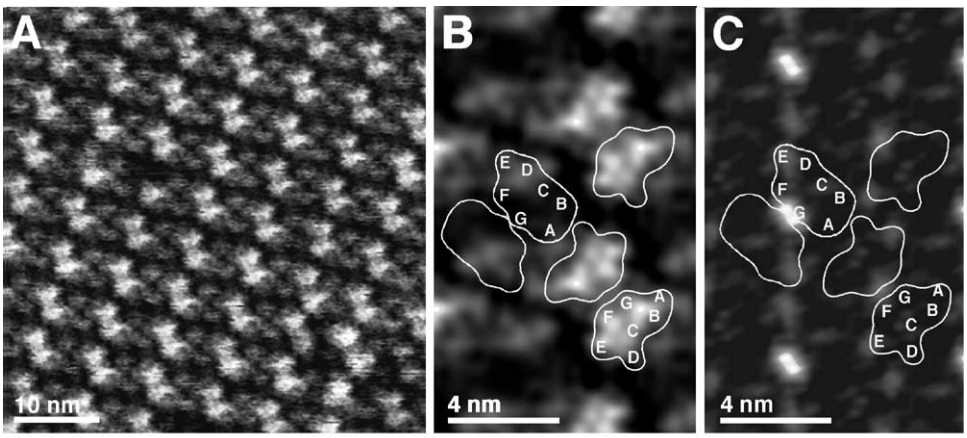

Fig. 17. Surface structure of bacteriorhodopsin depends on intermolecular interactions (Müller et al., 1999b). AFM topography (A) and average (B) of bacteriorhodopsin re-crystallized in presence of *n*-dodecyl trimethylammonium chloride (DTAC). Bacteriorhodopsin assembled into dimers which arrange into a rectangular lattice with a $p22_12_1$ symmetry and unit cell dimensions of $a = 5.8$ nm, $b = 7.4$ nm (Michel et al., 1980). Accordingly, the dimers alternately had their cytoplasmic surface or their extracellular surface facing the AFM stylus. The maximum height difference between the protrusions and the bilayer was 0.81 ± 0.09 nm. (C) The SD map of the average (B) shows structural areas exhibiting an enhanced variability. In contrast to bacteriorhodopsin trimers assembled into purple membrane (Fig. 16) the EF loops in this crystal form exhibited no enhanced SD and it was not possible to induce their conformational changes by slightly elevated forces.

Reassembly of bacteriorhodopsin showed that individual polypeptide loops connecting transmembrane helices changed their appearance and their physical properties. For example the EF loop, representing the most flexible regions of bacteriorhodopsin trimers of purple membrane, changed its conformation and lost its flexibility upon dimerization of bacteriorhodopsin and reassembly into an orthorhombic lattice (Fig. 17).

Although the observed structural changes may not significantly influence the proton pumping function of bacteriorhodopsin, they could be of crucial importance for transmembrane proteins whose surface regions are known to interact with other proteins. In particular, receptor proteins belonging to the G-protein-coupled family (Helmreich and Hofmann, 1996; Henderson et al., 1990) may be an important focus in future investigations.

6. Observing single protein assemblies

6.1. Assembly of proteins attached to a membrane

Annexins represent a family of structurally related proteins whose common property is calcium-dependent binding to negatively charged phospholipids (Kourie and Wood, 2000). Using time-lapse AFM the 2D assembly of annexin V on lipid layers was studied, allowing the growth of crystal domains to be observed (Reviakine et al., 1998). Individual defects observed within such a domain were randomly distributed and exhibited the size of one or several annexin trimers (Fig. 18; Reviakine et al., 2000). Surprisingly, these defects disappeared by increasing the incubation time, indicating that individual annexin trimers insert into single crystal defects from solution and associate with the lipid surface. This observation appears to be in contrast to the trimer assembly observed at the domain edges, where it is thought that annexin first associates with the lipid and then laterally assembles with other proteins. Both effects were found to be involved in the formation of large perfect 2D crystals.

Scheuring et al. used biotinylated lipids to bind streptavidin to the lipid monolayer formed at an air–water interface (Scheuring et al., 1999a). After this, the hydrophobic surface of the monolayer was transferred to the hydrophobic surface of highly oriented pyrolytic graphite (HOPG), which was used as support for AFM imaging. The AFM topographs revealed streptavidin molecules stably ordered into 2D crystals. Comparison of the topographs with the streptavidin structure demonstrated that they maintained their characteristic structure upon binding to the lipid monolayer and adsorption to the HOPG support.

6.2. Assembly of transmembrane proteins

The Schiff base of bacteriorhodopsin reacts with reagents such as hydroxylamine on illumination with light (Oesterhelt et al., 1974). This chemical reaction results in the breakage of the Schiff base bond between the bacteriorhodopsin and retinal, yielding the apoprotein bacterioopsin and retinaloxime. Consequently, the absorption maximum of purple membrane at 568 nm diminishes and the absorption maximum of retinaloxime at about 366 nm is observed (Oesterhelt et al., 1974). These spectral changes depend upon the illumination time and reflect the photobleaching process of purple membrane (Fig. 19A). The loss of the Schiff base bond leads to

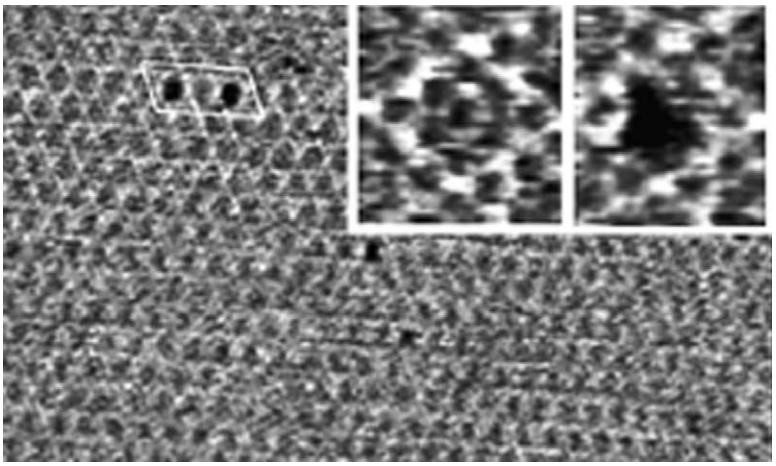

Fig. 18. Annexin V crystal grown on a lipid monolayer. The 2D crystal exhibited characteristic holes (parallelogram) that correspond to the absence of annexin V trimers. The insets show the molecular arrangement of the annexin V lattice with (left) and without (right) the annexin trimer located at the symmetry center of the lattice. The lateral dimension of the insets correspond to 25 nm × 30 nm. Enhancing the incubation time of free annexin V trimers resulted in a healing of individual crystal defects (Reviakine et al., 1998). The topographs were recorded in 150 mM NaCl, 2 mM $CaCl_2$, 3 mM NaN_3, 10 mM Hepes, pH 7.4, and exhibit a vertical scale of $\approx$3 nm (Image courtesy of A. Brisson, Bordeaux).

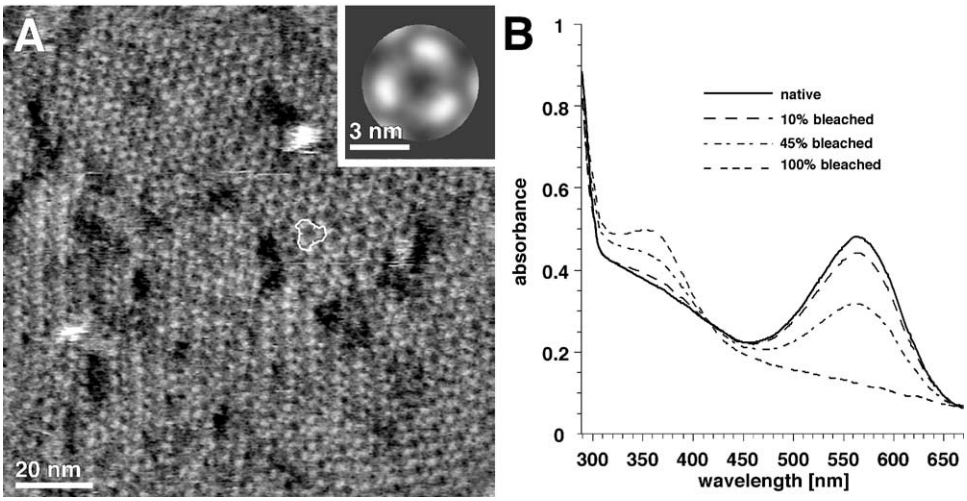

Fig. 19. Observing the disassembly of purple membranes. (A) Photobleached purple membrane imaged in buffer solution (10 mM Tris–HCl, pH 7.8, 150 mM KCl) using contact mode AFM. Upon exposure to light in the presence of hydroxylamine purple membranes lose their crystallinity. During disassembly of the purple membrane lattice the bacteriorhodopsin molecules remain assembled into trimers. Inset, three-fold symmetrized average calculated by single particle alignment of 172 disordered trimers as observed in (A). (B) The progress of photobleaching in the presence of hydroxylamine was monitored by absorption spectra and characterized by high-resolution AFM topographs (Möller et al., 2000). The topographs exhibit a full gray scale of 0.8 nm and are displayed as reliefs tilted by 5° (Image courtesy of C. Möller, Dresden).

structural changes in the apoprotein (Bauer et al., 1976; Becher and Cassim, 1977). As observed using AFM, the process of photobleaching (Fig. 19B) was associated with the breakdown of the purple membrane structure. Entirely bleached purple membrane lost most of its crystalline nature. High-resolution topographs showed the progressive separation of bacteriorhodopsin trimers, first along distinct lattice lines and later all over the membrane. Furthermore, the topographs showed that the bacterioopsin molecules remained assembled as trimers during the entire photobleaching process. Regeneration of the photobleached membranes into fully active purple membrane resulted in the renewed association of the bacteriorhodopsin trimers into a trigonal crystal. The regenerated membranes exhibited similar diameters, thickness and crystallinity to native purple membrane (Möller et al., 2000).

7. Observing protein function

AFM topographs of biomolecules are not only attractive because they reveal biomolecules in their most native state, but also because they exhibit an outstanding S/N ratio. Striking images have been recorded that show submolecular features of single biomolecules (Section 3). The following examples show that minute structural changes at protein surfaces can be detected with sufficient time resolution to monitor conformational changes involved in biological processes.

7.1. Conformational changes of a bacterial surface layer (S-layer)

The multiple functions of the hexagonally packed intermediate (HPI) layer from *Deinoccocus radiodurans* are still a matter of debate. HPI is a typical member of the outermost surface layers (S-layers) of bacteria (Sleytr, 1997; Sleytr et al., 1993). Evidence exists that the HPI-layer stabilizes the cell shape and functions as a protective barrier against hostile factors from the environment, which nutrients, solutes and waste products have to cross (Baumeister et al., 1988). Furthermore, it has been suggested that HPI-layers of two neighboring bacteria form connexons to enable cell–cell communication (Baumeister and Hegerl, 1986). As revealed by electron microscopy and crystallography studies (Baumeister et al., 1986; Engel et al., 1982; Rachel et al., 1986) the HPI-layer consists of a single type of protomer six of which form a pore.

As observed by AFM, it appears that individual pores of the inner HPI-layer surface can exist in unplugged (○) or plugged (□) conformation (Fig. 20). Time-lapse topographs show the pores to reversibly change their conformation (Müller et al., 1996a). After translational and angular alignment of single pores from the HPI-layer, a multivariate statistical analysis of 330 pores from 10 different topographs was performed. Fig. 20 (right) displays a montage of the calculated and six-fold symmetrized topographs of both conformations. The averages of the two major classes, both showing six subunits of the core and their emanating arms, exhibit either an 'open' or a 'closed' pore. The depression in the open conformation of the core was 1.8 ± 0.5 nm, the depression over the protrusion of the closed conformation was 1.0 ± 0.5 nm. This suggests that the HPI layer serves as a molecular sieve with open and closed states. Lack of functional and structural data, however, prevents confirmation of this hypothesis.

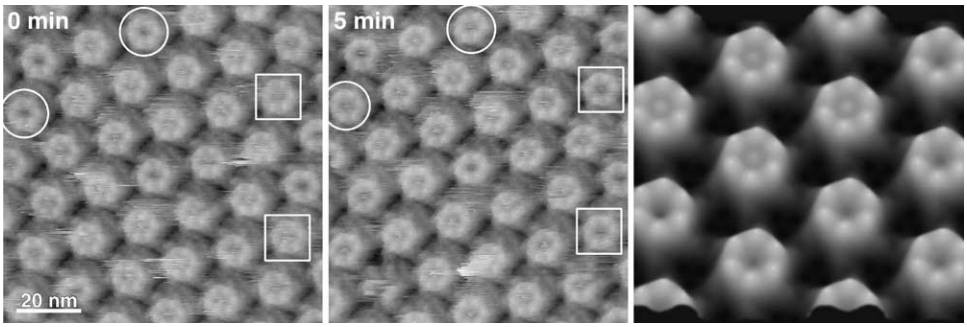

Fig. 20. Conformational change of individual pores of the HPI-layer. Left, inner surface of the HPI-layer as imaged by AFM in buffer solution. Protomers of the hexameric pores are clearly visible. Individual pores can exist in open (○) and plugged (□) conformations. Center, imaging of the same surface after 5 min demonstrates that some of the pores have changed their conformation. This conformational change is fully reversible and can be observed over hours. Right, surface relief of the averaged open and plugged conformations. The correlation averages of both the open and the closed conformations were six-fold symmetrized and then assembled in the montage. The distance between adjacent pores is 18 nm, the full gray level range of all contact mode topographs corresponds to 3 nm vertical distance. Average is displayed as a relief tilted by 5°.

7.2. Channel closure of OmpF porin

The outer membranes of Gram negative bacteria protect the cells from hostile factors such as proteolytic enzymes, bile salts, antibiotics, toxins, and low pH. The uptake of small nutrients and the release of metabolites are facilitated by passive pores, called porins. *E. coli* outer membranes contain approximately 10^5 porins per cell, which allow passage of small solutes < 600 Da (Nikaido and Vaara, 1985). In addition to nutrients, antibiotics which need to cross the outer membrane for binding to their targets also diffuse through these aqueous pores (Nikaido, 1989). Conductance measurements have shown that the porin OmpF trimer exists in open or closed states, depending on the transmembrane potential (Lakey, 1987; Schindler and Rosenbusch, 1978). The critical voltages ($V_c \approx 90$ mV for OmpF porin) above which channels close is affected by the pH (Todt et al., 1992), membrane-derived oligosaccharides (Delcour et al., 1992), polysaccharides (Schindler and Rosenbusch, 1981), polycations (dela Vega and Delcour, 1995), and pressure (Le Dain et al., 1996). Although the structures of several porins have been solved (Cowan et al., 1992; Schirmer, 1998; Weiss et al., 1991), the nature of channel closure is poorly understood.

The structurally and functionally well characterized bacterial porin OmpF is an excellent structure to assess in depth the ability of the AFM to monitor conformational changes. The short polypeptide loops at the periplasmic surface (Figs. 1 and 2) and the long loops at the extracellular surface (Fig. 21) are observed on individual porin trimers in the AFM topographs. Variable extracellular loops protrude by 1.3 nm above the bilayer at neutral pH. Three conditions have been demonstrated to induce the collapse of this flexible domain towards the trimer center, to form a structure with a height of only 0.6 nm (Müller and Engel, 1999): (i) application of an electric potential > 200 mV across the membrane, (ii) generation of a K^+ gradient > 0.3 M

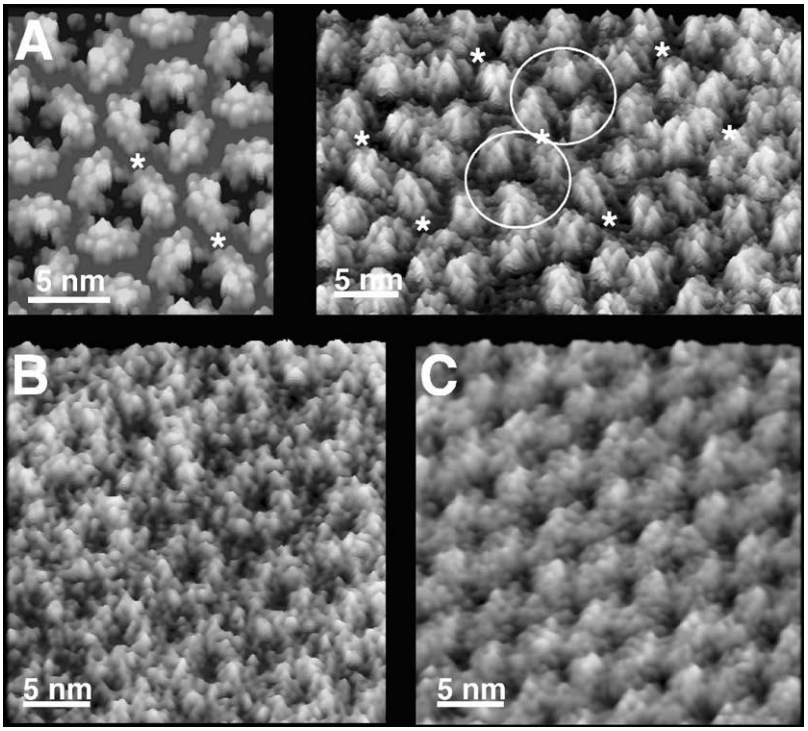

Fig. 21. Conformational changes of porin OmpF. (A) The comparison between atomic model (left) and unprocessed topograph (right) illustrates the extracellular loops protruding 1.3 nm from the bilayer to be flexible. The asterisks mark the two-fold symmetry axis of the rectangular unit cells housing two porin trimers. (B) pH-dependent conformational change of the extracellular surface. At pH $\leqslant$ 3 the flexible loops reversibly collapse towards the center of the trimer thereby reducing their height by 0.6 nm. (C) Conformational change of porin induced by an electrolyte gradient. The monovalent electrolyte gradient across the membrane was $>$300 mM. Similar to the pH-dependent conformational change, the extracellular domains reversibly collapsed onto the porin surface (Müller and Engel, 1999). Topographs exhibit a vertical range of 1.5 nm (A), and 1.2 nm (B, C) and are displayed as relief tilted by 5°.

(Fig. 21B), and (iii) acidic pH ($\leqslant$3) (Fig. 21C). The last condition suggests a protective function: *E. coli* cells passing through the acidic milieu of a stomach may survive longer by closing the outer membrane pores. The first condition, however, is compatible with results from black lipid membrane and patch clamping experiments which demonstrated that porin acts as a voltage gated channel (Delcour, 1997; Klebba and Newton, 1998).

7.3. Conformational changes of gap junction

In gap junctions *connexins* oligomerize to form *connexons*, which link up in pairs that bridge the extracellular space between two opposed plasma membranes. Typically, several thousand connexons aggregate in the membrane plane forming a junctional plaque with distinct boundaries. The paired connexon establish a transmembrane channel (also called an intercellular channel) mediating intercellular transport and signaling. Early AFM experiments showed that the AFM

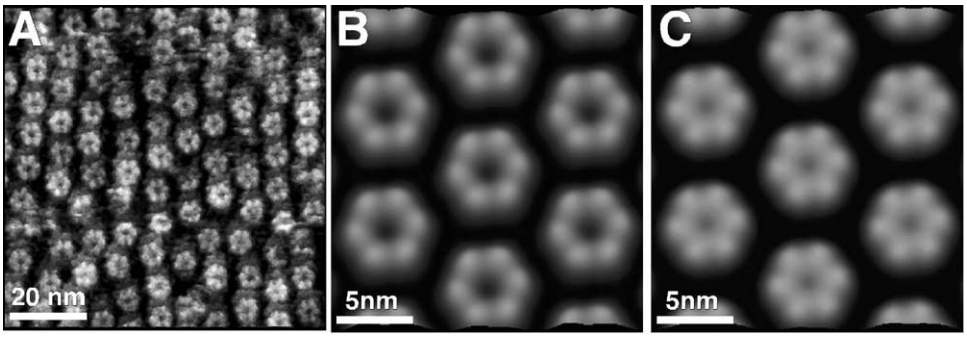

Fig. 22. Ca^{2+} induced conformational change of the extracellular connexon surface. (A) Extracellular connexon surface imaged in buffer solution (5 mM Tris, 1 mM EGTA and 1 mM PMSF). (B, C) Averaged topographs of extracellular connexon surfaces recorded in absence of (B) and with 0.5 mM Ca^{2+} (C). These contact mode AFM topographs were recorded using applied forces of 50 pN, and are displayed with a vertical scale of 2 nm.

stylus can be used to dissect the gap junctions (Hoh et al., 1991) and to image the extracellular connexon surface (Hoh et al., 1993). Improved biochemical preparation methods (Hand et al., 2001) and imaging conditions (Müller et al., 1999a) allowed the connexon surface to be imaged reproducibly at submolecular resolution (Fig. 22A). Intact connexon exhibit six subunits surrounding the entrance of the transmembrane channel.

Experiments in several cell systems measuring cell–cell coupling have shown that Ca^{2+} ions decrease or suppress electrical coupling mediated by gap junctions. Electrophysiological experiments have shown that high concentration of calcium ions in the external medium close non-junctional gap junction hemichannels (Cx43: Li et al. (1996); Cx46: Pfahnl and Dahl (1999); and Cx26: Kamermans et al. (2001)). Under similar experimental conditions AFM has been used to show the physical movement of connexins associated with the physiological closure of the connexon channel (Fig. 22C). From the topographs it is evident that the channel entrance of the pore significantly decreased in diameter from 1.5 ± 0.3 to 0.6 ± 0.3 nm ($n = 47$) (Figs. 22B and C). This conformational change was fully reversible and could be repeated over 5 times within a time range of 2 h.

7.4. Working cycle of a chaperone

GroEL shows the tendency to orientate with its upper cavity towards the scanning AFM tip when adsorbed onto freshly cleaved mica (Mou et al., 1996a, b). Thus, by coating the tip with a substrate, the interaction of the substrate with the GroEL cavity can be directly assessed. Using this approach, Vinckier et al. showed interaction forces of citrate synthase from *Saccharomyces cerevisiae* and of RTEM β-lactamase from *E. coli* with bacterial GroEL to decrease in the presence of ATP but to increase when the proteins are denaturated (Vinckier et al., 1998).

Using the same preparation procedure Hansma et al. added GroES to GroEL adsorbed onto the supporting mica surface (Viani et al., 2000). The proteins were observed to associate in the presence of 2 mM ADP, thereby forming a functional unit. Development of a fast scanning small

cantilever AFM allowed Hansma et al. to detect force variations in the MHz range with pico-Newton sensitivity (Viani et al., 1999). Using this microscope the reversible binding and dissociation of GroEL and GroES were observed in real time in the presence of 2 mM ADP and 2 mM Mg-ATP. These examples demonstrate that AFM enables the measurement of interactions involved in protein folding, and that various functions of chaperonins in protein folding may be monitored at the single molecule level in the future.

8. Measuring electrostatic properties

Shortly after its invention the capability of the AFM to measure intermolecular surface forces in biological systems was demonstrated (Butt, 1991b; Butt et al., 1995; Ducker et al., 1991). To this end, the AFM tip (or probe) was brought close to the biological object while recording the deflection of the AFM cantilever. The resulting force spectrum was then analyzed to unravel the interactions which had occurred. Electrostatic interactions measured using AFM are most commonly covered by the continuum DLVO theory (Israelachvili, 1991). Here, the interplay between the electrostatic double layer (EDL) and the van der Waals force is described, neglecting effects of ion radii, hydration forces, steric forces and specific interactions. Ion clouds compensating the surface charges of a surface start to overlap as soon as two surfaces are separated by a few tens of nm. This results in an osmotic pressure between the two surfaces. At sufficiently short distances, however, the attractive van der Waals force supersedes the repulsive EDL force. The total force F_{DLVO}, between a sphere of radius R interacting with a planar surface is given by (Israelachvili, 1991)

$$F_{\mathrm{DLVO}}(z) = F_{\mathrm{el}}(z) + F_{\mathrm{vdW}}(z) = \frac{4\pi\sigma_{\mathrm{m}}\sigma_{\mathrm{t}}R\lambda_{\mathrm{D}}}{\varepsilon_{\mathrm{e}}\varepsilon_0}\mathrm{e}^{-z/\lambda_{\mathrm{D}}} - \frac{H_{\mathrm{a}}R}{6z^2}, \tag{1}$$

where σ_{m} and σ_{t} are the surface charge densities of membrane and tip, ε_0 is the permittivity of the free space, ε_{e} is the dielectric constant, H_{a} is the Hamaker constant, and z is the distance between the two surfaces. The Debye length λ_{D} characterizes the exponential decrease of the potential resulting from screening the surface charges with electrolytes, with $\lambda_{\mathrm{D}} = 0.304/\sqrt{e_{\mathrm{C}}}$ nm for monovalent and $0.174/\sqrt{e_{\mathrm{C}}}$ nm for divalent (1:2 or 2:1) electrolytes. Hence, if the electrolyte composition and pH of the buffer solution are known, the measured exponential decay of the osmotic force can be fitted to reveal the surface charge density of the object (Israelachvili, 1991).

8.1. Detecting surface charges of membranes

More than one decade ago Butt performed initial experiments in which he measured the electrostatic repulsion of native biological membranes using AFM in the force spectroscopy mode (Butt, 1991a, b). A surface charge of –0.05 C/m^2 was detected for a purple membrane fitting the experimental data with equations derived by the DLVO theory (Butt, 1992). These repulsive forces potentially influence the contrast mechanism of the AFM during imaging a biological sample (Heinz and Hoh, 1999; Manne and Gaub, 1995; Müller and Engel, 1997; Rotsch and Radmacher, 1997). If the nature of these forces is known, they could be adjusted, by either changing the pH or by the electrolyte concentration of the buffer solution.

The AFM probe can also be used as a sensor to probe the charges of biological surfaces immersed in buffer solution (Butt et al., 1995). Here, the EDL force (Israelachvili, 1991) interacting between the charged probe and charged regions of the biological sample can contribute significantly to the AFM topograph recorded (Müller and Engel, 1997; Rotsch and Radmacher, 1997) and can be tuned by the electrolyte concentration and the pH of the buffer solution. The DLVO theory describes the exponential decay of the EDL force as a function of the surface separation (Israelachvili, 1991). While AFM probes have been used to measure the average surface charges from force-separation curves (Butt, 1991b; Ducker et al., 1991), surface charge maps have been obtained at 40 nm lateral resolution by recording force-separation curves at each pixel of the sampled surface (Heinz and Hoh, 1999; Rotsch and Radmacher, 1997).

8.2. Detecting the electrostatic potential of a transmembrane channel

OmpF porin located in the outer membrane of *E. coli* exists as stable trimeric structures. The 340 aa long polypeptide of the OmpF monomer is folded into 16 antiparallel β-strands that form a large hollow transmembrane β-barrel structure (Cowan et al., 1992). An infolding loop forms the eyelet of each barrel constricting the passage of ions and hydrophilic solutes up to an exclusion size of ≈ 600 kDa (Nikaido and Saier, 1992; Schirmer, 1998). The translocation rate of the channel and solute concentration gradient across the membrane show a linear relation. The ion selectivity of the pore, however, increases with decreasing electrolyte concentration (Schirmer and Phale, 1999). This selectivity is altered by modification of the charged amino acids of the pore lining (Saint et al., 1996), which are thought to produce a characteristic electric field at the pore constriction (Cowan et al., 1992; Weiss et al., 1991). Hence, it has been suggested that the charges of the porin constriction primarily modulate the pore selectivity (Klebba and Newton, 1998; Schirmer, 1998). However, the electrostatic potential at the entrance of the OmpF porin channel was not explored in these calculations.

To map the electrostatic potential of native porin OmpF experimentally, high-resolution AFM topographs were recorded under variable electrostatic conditions (Philippsen et al., 2002). The electrostatic potential of the protein channel was then decomposed by subtracting topographs recorded at different electrostatic contributions (Figs. 23A–C). Figs. 23D and E show the superimposition of the AFM topograph (brown yellow) and of the electrostatic potential (red to white). The electrostatic potentials represent difference maps calculated from topographs recorded at different electrostatic contributions, 300 and 50 mM KCl (Fig. 23D), and 300 and 100 mM KCl (Fig. 23E). The results clearly show that the porin establishes a negative electric potential at its pore entrance, which increases with decreasing electrolyte concentration. It is assumed that this potential might be responsible for the pore selectivity against negatively charged ions.

9. Controlled manipulation of single proteins

As well as imaging the native structure of biological macromolecules, the AFM stylus can also be used to manipulate single molecules (Clausen-Schaumann et al., 2000; Fisher et al., 2000; Rief et al., 2000). As demonstrated within the past 5 years, the combination of AFM imaging and manipulation allows precise and controlled modifications of biological systems from a macroscopic scale down to the scale of individual molecules (Fotiadis et al., 2002). The first

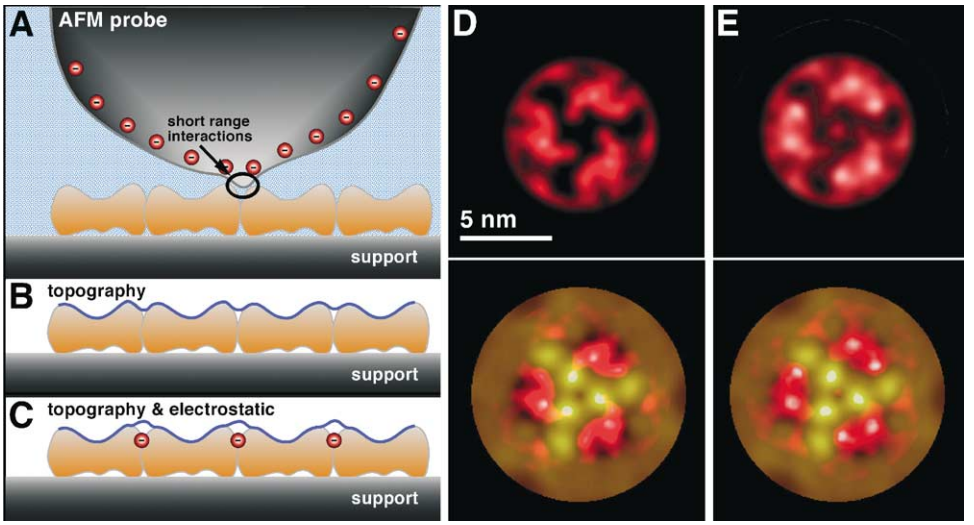

Fig. 23. Mapping the electrostatic potential of the OmpF porin channel. (A) Principle of recording topographs at variable electrostatic contribution. (B) Scanning a negatively charged AFM tip (silicon nitride) over an electrically neutral surface reveals the true topography. (C) In case of discrete negative charges the AFM tip detects local electrostatic repulsions. The resulting topograph represents a mixture of structural and electrostatic information, which can be decomposed by subtracting the topograph recorded without from that recorded with electrostatic contributions. Difference maps between topographs recorded of the periplasmic OmpF porin surface at 100 and 300 mM KCl and at 50 (D) and 300 mM KCl (E). As becomes evident, the main differences between porin trimers recorded at different electrolyte concentrations are located at the entrances of the transmembrane pore. The color scale shaded from white (highest difference) over red (high difference) to black (difference < 0.05 nm) corresponds to a vertical height of 0.3 nm (D) and of 0.5 nm (E). Lower panels show the superimposition of the averaged topograph (colored brown-gold) and the electrostatic potential.

manipulation on biomolecules achieved with the AFM was performed on genetic material (Hansma et al., 1994a). DNA adsorbed to mica could be cut, both in air (Henderson, 1992; Vesenka et al., 1992) and in propanol (Hansma et al., 1992), by increasing the applied force to about 5 nN while scanning an area of 30 nm $\times$ 30 nm.

9.1. Manipulation of individual proteins

Imaging the pigment-containing reaction center PSI (see Section 3.4) with the AFM has resolved the three extrinsic subunits PsaC, -D, and -E which protrude 3.5 nm above the lipid bilayer on the stromal PS I surface (Fig. 24A). Using the AFM tip as a 'nanotweezer', single extrinsic subunits were removed by repetitive scanning. As a result the underlying molecular interfaces were exposed and accessible for structural analysis at high resolution (Fig. 24B) (Fotiadis et al., 1998).

9.2. Imaging, manipulating and detecting forces of individual proteins

Structural, chemical and morphological studies have shown that S-layers are one of the most primitive membrane structures developed during evolution. They cover the cell surface

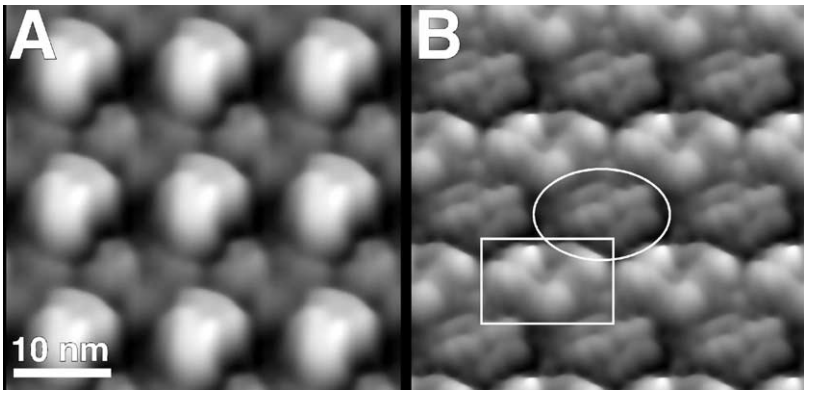

Fig. 24. Dissection of cyanobacterial PSI complexes. (A) AFM average of a 2D PSI crystal containing all extrinsic proteins. The high protrusions arise from the extrinsic subunits PsaC, PsaD, and PsaE located on the stromal side. The PSI complexes are orientated up and down in the membrane ($p12_12$ symmetry) exposing, therefore, the stromal and the lumenal surface. (B) Average of the crystal depleted of all extrinsic proteins, which disappeared upon repetitive scanning of the same area. The stromal surface depleted of the extrinsic subunits unveils the topography of the reaction center core (ellipse). The lumenal surface is marked by a rectangle. The contact mode topographs were recorded in buffer solution (300 mM KCl, 20 mM Tris–HCl, pH 7.8), exhibit vertical brightness ranges of 3.5 nm (A) and 1.7 nm (B) and are displayed as reliefs tilted by 5°.

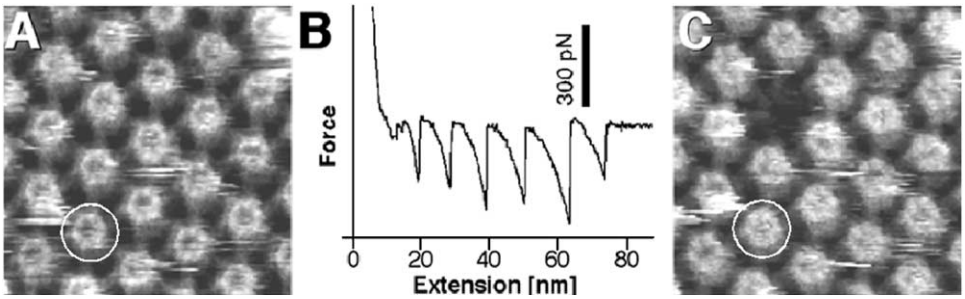

Fig. 25. Unzipping a pore of the S-layer from *D. radiodurans*. (A) Control AFM topograph of the inner surface. (B) The force–extension curve recorded from this inner surface region shows a sawtooth like pattern with six force peaks of about 300 pN. (C) The same inner surface area imaged after recording the force curve; a molecular defect of the size of a hexameric HPI protein complex has clearly been created. Even within these experiments it was possible to observe the reversible switch of the hexameric pores from a plugged to an unplugged conformation (compare Fig. 20). Brightness range corresponds to 3 nm. Imaging and force spectroscopy were performed in buffer solution (150 mM KCl, 20 mM $MgCl_2$, 10 mM Tris–HCl, pH 7.8).

completely, are usually composed of a single protein and are endowed with the ability to assemble into monomolecular arrays by an entropy driven process (Sleytr et al., 1993). Experimental results indicate that the integrity of the S-layer lattice is maintained by different combinations of weak bonds, which are stronger than those binding to the underlying cell envelope component (Sleytr, 1997; Sleytr et al., 1993).

The inner surface of the HPI-layer was imaged (Fig. 25A) to gain insight into the interaction forces holding together the assembly (see Section 7.1). Most importantly for later structural

correlation, the resolution of the topograph was sufficient to resolve the individual subunits of the hexameric pores and of their emanating arms. After imaging the HPI-layer, the AFM stylus was attached to an individual protomer by enforced stylus-sample contact to allow single molecule force spectroscopy experiments (Fig. 25B). As visible from the force spectroscopy curve six strong adhesion peaks of the inner HPI-layer surface to the silicon nitride stylus were observed on retracting the stylus. This indicates that a molecular structure bridged the gap between the AFM stylus and the HPI-layer. It is likely that this molecular bridge is mediated by the hydrophobic sequence segments near the N-terminus which itself also carries an alkyl moiety, a region thought to interact with the outer membrane (Peters et al., 1987). Imaging of the HPI-layer after recording force–extension curves allowed adhesion forces to be correlated with structural alterations (Fig. 25C). The entire HPI hexamer was missing with each adhesion peak standing for the removal of one protomer from the layered assembly. Using this approach, individual protomers of the HPI-layer were removed at average pulling forces of ≈ 310 pN.

9.3. Imaging and unfolding of single proteins

To measure the intramolecular interaction forces within bacteriorhodopsin, AFM and single-molecule force spectroscopy were applied similarly to the procedure described above. After imaging the cytoplasmic purple membrane surface (Fig. 26A), the AFM probe was pushed towards the purple membrane surface exerting a force of about 1 nN. When the two surfaces were separated, force–extension curves like those shown in Fig. 26B were recorded. The force–extension curve showed a molecular bridge persisting to distances of 75 nm, corresponding to the length of an entirely unfolded bacteriorhodopsin (248 aa). The analysis of single-molecule force spectra unraveled the individuality of their unfolding pathways. Helices G and F as well as helices E and D always unfolded pairwise at pH 7.8, while helices B and C occasionally unfolded one after the other. Experiments with cleaved bacteriorhodopsin loops revealed the origin of these differences to be the result of the stabilization of helix B by neighboring helices.

10. Perspectives

Since the 1980s, when Binnig, Gerber and Rohrer unveiled the scanning tunneling microscope (STM; Binnig et al., 1982), the surface structure and electronic properties of conducting samples have been explored with atomic resolution. The application of STM to non-conducting surfaces such as most biological systems, however, was extremely limited. A few years later in 1986 Binnig, Quate and Gerber introduced AFM (Binnig et al., 1986), allowing the detection of conducting and non-conducting surface structures at similar resolution. Most importantly for biologists, the AFM can be operated in aqueous solutions under controlled temperatures. The potential of this technique for the investigation of biological applications, was thus early recognized (Drake et al., 1989). A key accomplishment in creating a user-friendly AFM was the development of a fluid cell and laser-based detection system (Hansma et al., 1994b) allowing biological samples to be investigated under physiologically relevant conditions.

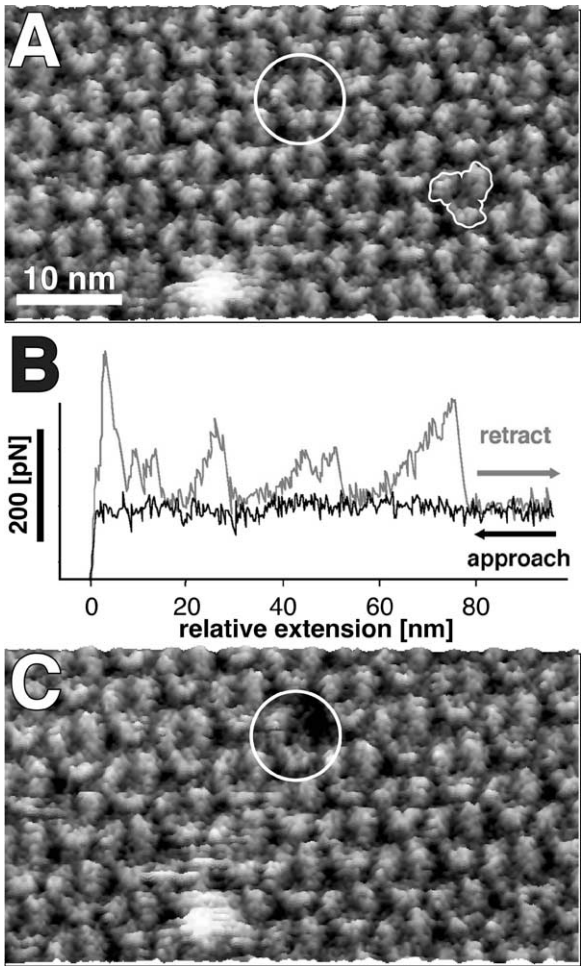

Fig. 26. Controlled unfolding of individual bacteriorhodopsins from native purple membrane. (A) AFM topograph of the cytoplasmic purple membrane surface. The bacteriorhodopsin molecules forming trimers (outlined trimer) are clearly visible. To select an individual protein we zoomed in (circled area) by reducing the pixel number and frame size. After positioning the AFM probe was kept in contact with the protein surface for about ≈ 1 s. Most of the extension curves recorded on the cytoplasmic surface showed no adhesion peaks. However, 5% of the adhesion curves showed discontinuous adhesion forces similar to that shown in (B). The length of the force spectra extended to distances up to 75 nm, corresponding to the length of one entirely unfolded protein. (C) After recording the force spectra, a topograph of the manipulated surface area was captured. The image clearly showed one single bacteriorhodopsin monomer to be missing (○). Topographs were recorded in buffer solution (300 mM KCl, 10 mM Tris–HCl, pH 7.8) using contact mode AFM, exhibit a brightness range of 1.5 nm, and are displayed as relief tilted by 5°.

10.1. High-speed AFM

Because of mechanical constraints of the AFM, the recording time of a high-resolution topograph of single molecules currently corresponds to a minimum of ≈ 60 s. To speed up this scanning process Hansma and coworkers invented soft and short AFM cantilevers exhibiting a much higher resonance frequency (Viani et al., 2000, 1999). Ando et al. showed that in

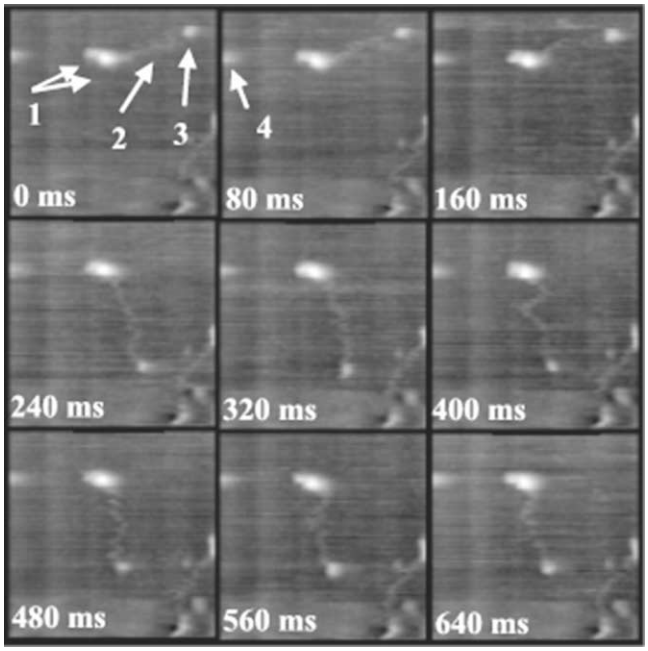

Fig. 27. High-speed time-lapse AFM of myosin V adsorbed onto mica. The head/neck regions (1), the long tail (2) and the globular tail (3) are marked by arrows. After some topographs were recorded, the long tail and the globular tail change their positions. The frame rate of these images was 12.5/s. Topographs were recorded in 25 mM KCl, 25 mM Imidazole, 2 mM MgCl2, 2 mM ATP, 1 mM EGTA, at pH 7.2 and exhibit a size of 240 nm × 240 nm (Image courtesy of T. Ando, Kanazawa).

combination with high-speed scanners these small cantilevers can be used to enhance the scanning speed of native myosin molecules by a factor of $\approx$300–400 (Ando et al., 2001) (Fig. 27). With this fast speed AFM, about 10–15 frames of a single molecule can be recorded within a second. Most biological processes, however, occur over much shorter time scales. Because of physical limitations of the current cantilever design new concepts will be required to allow higher spatial and temporal resolution of the conformational changes and dynamics of biological systems in real time.

10.2. Improved force control

Operation of the AFM in contact mode, tapping mode, or dynamic mode induces forces upon biological samples. Surface topographs of single proteins show discrepancies compared to their atomic models when imaged at forces >150 pN (Heymann et al., 1999; Müller et al., 1995, 1997b; Scheuring et al., 1999b). When imaging at a lateral resolution <1 nm the AFM tip and the macromolecule interact locally over a small surface area $<1\,\mathrm{nm}^2$ (Engel et al., 1997) and the surface pressure is relatively high. Consequently, the molecular deformation of soft biological samples is more sensitive to sharp AFM tips, which are required to observe single molecules at submolecular resolution. However, because the precision of the force applied to the AFM

cantilever depends on external factors such as thermal drift, the operator is currently challenged to compensate this drift manually. This effect is independent of the imaging mode used (Möller et al., 1999, 1999a). Future generations of AFM, equipped with an automatic adjustment of the applied force will produce more stable imaging conditions of the sample and will allow even lower and more accurate force measurements.

10.3. Simultaneous detection of optical signals

The next generation of probe microscopy instruments will combine several techniques. For example, capabilities in single-molecule fluorescence (Weiss, 1999, 2000), and in fluorescence resonance energy transfer (FRET) that can measure changes in relative distances on the 2–8 nm scale (Selvin, 2000), might be combined with AFM imaging to generate new quantitative data. Single biological machineries could be simultaneously imaged by AFM and characterized by fluorescence detection. Alternatively the near-field scanning optical microscope (NSOM), which offers improved resolution over standard optical tools, may be combined with an AFM to observe single molecules (Heinzelmann and Pohl, 1994; Lewis et al., 1999; Meixner and Kneppe, 1998). Such approaches would allow the characterization of functional transitions and molecular interactions of single molecules in a heterogeneous environment. The molecular arrangement of assembled proteins can be resolved at a special resolution of <1 nm. Such detailed information will promote the understanding of protein assembly through more accurate models of protein complexes and molecular modeling of the protein arrangement and will provide insights into mechanisms that drive intermolecular interactions in cellular systems.

10.4. Simultaneous detection of multiple parameters

Instruments, which probe multiple properties of surfaces have proliferated after the initial introduction of STM and AFM. Currently these scanning probe microscopy (SPM) techniques are mainly applied to chemical and physical problems. Biologists have to familiarize themselves with microscopes enabling the detection of thermal, chemical, electrochemical, elastic, molecular and electronic properties from cells to single molecules. Moreover, sophisticated procedures allow the AFM probe to be functionalized (Hafner et al., 2001; Schmitt et al., 2000) as a nanotweezer and to touch, grab and manipulate individual molecules (Fotiadis et al., 2002). The current challenge is not only in operating such instruments but also in understanding what is observed by their use. This strongly interdisciplinary field requires familiarity with molecular biology, biochemistry, biophysics, chemistry, surface science, and physics.

10.5. Imaging and nanomanipulation of single proteins

The controlled imaging and manipulation of single proteins introduces many possibilities to study molecular interactions that drive important biological processes. Extensive studies and improved analysis of unfolding events have led to detailed insights into the unfolding process of bacteriorhodopsin. In addition to the dominant pairwise unfolding the intramolecular forces required to unfold every transmembrane α-helix as well as individual polypeptide loops were detected (Müller et al., 2002). As a next step it may be investigated as to which factors determine

the stability of membrane proteins and of their secondary structure elements. Of similar importance, however, is to characterize interactions responsible for the functionally related assembly of proteins under physiological conditions. For example, such approaches will assist understanding mechanisms of dynamic raft formation, signal transduction, and the smallest functional entities of complementary proteins.

References

Agre, P., Preston, G.M., Smith, B.L., Jung, J.S., Raina, S., Moon, C., Guggino, W.B., Nielsen, S., 1993. Aquaporin CHIP: the archetypal molecular water channel. Am. J. Physiol. 265, F463–F476.

Ando, T., Kodera, N., Takai, E., Maruyama, D., Saito, K., Toda, A., 2001. A high-speed atomic force microscope for studying biological macromolecules. Proc. Natl. Acad. Sci. USA 98, 12468–12472.

Baker, A.A., Helbert, W., Sugiyama, J., Miles, M.J., 1997. High-resolution atomic force microscopy of native valonia cellulose I microcrystals. J. Struct. Biol. 119, 129–138.

Baker, A.A., Helbert, W., Sugiyama, J., Miles, M.J., 2000. New insight into cellulose structure by atomic force microscopy shows the i(alpha) crystal phase at near-atomic resolution. Biophys. J. 79, 1139–1145.

Baldwin, J.M., 1993. The probable arrangement of the helices in G protein-coupled receptors. EMBO J. 12, 1693–1703.

Bamberg, E., Tittor, J., Oesterhelt, D., 1993. Light-driven proton or chloride pumping by halorhodopsin. Proc. Natl. Acad. Sci. USA 90, 639–643.

Bauer, P.-J., Dencher, N.A., Heyn, M.P., 1976. Evidence for chromophore–chromophore interactions in the purple membrane from reconstitution experiments of the chromophore-free membrane. Biophys. Struct. Mechanism 2, 79–92.

Baumeister, W., Hegerl, R., 1986. Can S-layers make bacterial connexons? FEMS Microbiol. Lett. 36, 119–125.

Baumeister, W., Barth, M., Hegerl, R., Guckenberger, R., Hahn, M., Saxton, W.O., 1986. Three-dimensional structure of the regular surface layer (HPI layer) of *Deinococcus radiodurans*. J. Mol. Biol. 187, 241–253.

Baumeister, W., Wildhaber, I., Engelhardt, H., 1988. Bacterial surface proteins: some structural, functional and evolutionary aspects. Biophys. Chem. 29, 39–49.

Baumeister, W., Walz, J., Zuhl, F., Seemuller, E., 1998. The proteasome: paradigm of a self-compartmentalizing protease. Cell 92, 367–380.

Becher, B., Cassim, J.Y., 1977. Effects of bleaching and regeneration on the purple membrane structure of *Halobacterium halobium*. Biophys. J. 19, 285–297.

Belrhali, H., Nollert, P., Royant, A., Menzel, C., Rosenbusch, J.P., Landau, E.M., Pebay-Peyroula, E., 1999. Protein, lipid and water organization in bacteriorhodopsin crystals: a molecular view of the purple membrane at 1.9 a resolution. Struct. Fold. Des. 7, 909–917.

Binnig, G., Rohrer, H., Gerber, C., Weibel, E., 1982. Tunneling through a controllable vacuum gap. Appl. Phys. Lett. 40, 178.

Binnig, G., Quate, C.F., Gerber, C., 1986. Atomic force microscope. Phys. Rev. Lett. 56, 930–933.

Borgnia, M., Nielsen, S., Engel, A., Agre, P., 1999. Cellular and molecular biology of the aquaporin water channels. Annu. Rev. Biochem. 68, 425–458.

Butt, H.-J., 1991a. Electrostatic interaction in atomic force microscopy. Biophys. J. 60, 777–785.

Butt, H.-J., 1991b. Measuring electrostatic, van der Waals, and hydration forces in electrolyte solutions with an atomic force microscope. Biophys. J. 60, 1438–1444.

Butt, H.-J., 1992. Measuring local surface charge densities in electrolyte solutions with a scanning force microscope. Biophys. J. 63, 578–582.

Butt, H.-J., Jaschke, M., Ducker, W., 1995. Measuring surface forces in aqueous solution with the atomic force microscope. Bioelect. Bioenerg. 38, 191–201.

Calamita, G., Kempf, B., Bonhivers, M., Bishai, W.R., Bremer, E., Agre, P., 1998. Regulation of the *Escherichia coli* water channel gene aqpZ. Proc. Natl. Acad. Sci. USA 95, 3627–3631.

Cheung, C.L., Hafner, J.H., Lieber, C.M., 2000. Carbon nanotube atomic force microscopy tips: direct growth by chemical vapor deposition and application to high-resolution imaging. Proc. Natl. Acad. Sci. USA 97, 3809–3813.

Clausen-Schaumann, H., Seitz, M., Krautbauer, R., Gaub, H.E., 2000. Force spectroscopy with single bio-molecules. Curr. Opin. Chem. Biol. 4, 524–530.

Cowan, S.W., Schirmer, T., Rummel, G., Steiert, M., Ghosh, R., Pauptit, R.A., Jansonius, J.N., Rosenbusch, J.P., 1992. Crystal structures explain functional properties of two *E. coli* porins. Nature 358, 727–733.

Czajkowsky, D., Allen, M., Elings, V., Shao, Z., 1998a. Direct visualization of surface charge in aqueous solution. Ultramicroscopy 74, 1–5.

Czajkowsky, D.M., Sheng, S., Shao, Z., 1998b. Staphylococcal alpha-hemolysin can form hexamers in phospholipid bilayers. J. Mol. Biol. 276, 325–330.

Czajkowsky, D.M., Iwamoto, H., Cover, T.L., Shao, Z., 1999. The vacuolating toxin from *Helicobacter pylori* forms hexameric pores in lipid bilayers at low pH. Proc. Natl. Acad. Sci. USA 96, 2001–2006.

dela Vega, A.L., Delcour, A.H., 1995. Cadaverine induces closing of *E.coli* porins. EMBO J. 14, 6058–6065.

Delcour, A., 1997. Function and modulation of bacterial porins: insights from electrophysiology. FEMS Microbiol. Lett. 151, 115–123.

Delcour, A.H., Adler, J., Kung, C., Martinac, B., 1992. Membrane-derived oligosaccharides (MDO's) promote closing of an *E. coli* channel. FEBS 304, 216–220.

Dorn, I., Eschrich, R., Seemüller, E., Guckenberger, R., Tampé, R., 1999. High-resolution AFM-imaging and mechanistic analysis of the 20 S proteasome. J. Mol. Biol. 288, 1027–1036.

Drake, B., Prater, C.B., Weisenhorn, A.L., Gould, S.A.C., Albrecht, T.R., Quate, C.F., Cannell, D.S., Hansma, H.G., Hansma, P.K., 1989. Imaging crystals, polymers, and processes in water with the atomic force microscope. Science 243, 1586–1588.

Ducker, W.A., Senden, T.J., Pashley, R.M., 1991. Direct measurements of colloidal forces using an atomic force microscope. Nature 353, 239–241.

Engel, A., Müller, D.J., 2000. Observing single biomolecules at work with the atomic force microscope. Nat. Struct. Biol. 7, 715–718.

Engel, A., Baumeister, W., Saxton, W., 1982. Mass mapping of a protein complex with the scanning transmission electron microscope. Proc. Natl. Acad. Sci. USA 79, 4050–4054.

Engel, A., Schoenenberger, C.-A., Müller, D.J., 1997. High-resolution imaging of native biological sample surfaces using scanning probe microscopy. Curr. Opin. Struct. Biol. 7, 279–284.

Engelbrecht, S., Junge, W., 1997. ATP synthase: a tentative structural model. FEBS Lett. 414, 485–491.

Essen, L.-O., Siegert, R., Lehmann, W.D., Oesterhelt, D., 1998. Lipid patches in membrane protein oligomers: crystal structure of the bacteriorhodopsin–lipid complex. Proc. Natl. Acad. Sci. USA 95, 11673–11678.

Fedorov, A.N., Baldwin, T.O., 1997. GroE modulates kinetic partitioning of folding intermediates between alternative states to maximize the yield of biologically active protein. J. Mol. Biol. 268, 712–723.

Ferguson, S.J., 2000. ATP synthase: what determines the size of a ring? Curr. Biol. 10, R804–R808.

Fisher, T.E., Oberhauser, A.F., Carrion-Vazquez, M., Marszalek, P.E., Fernandez, J.M., 1999. The study of protein mechanics with the atomic force microscope. Trends Biochem. Sci. 24, 379–384.

Fisher, T.E., Marszalek, P.E., Fernandez, J.M., 2000. Stretching single molecules into novel conformations using the atomic force microscope. Nat. Struct. Biol. 7, 719–724.

Fotiadis, D., Müller, D.J., Tsiotis, G., Hasler, L., Tittmann, P., Mini, T., Jenö, P., Gross, H., Engel, A., 1998. Surface analysis of the photosystem I complex by electron and atomic force microscopy. J. Mol. Biol. 283, 83–94.

Fotiadis, D., Hasler, L., Müller, D.J., Stahlberg, H., Kistler, J., Engel, A., 2000. Surface tongue-and-groove contours on lens MIP facilitate cell-to-cell adherence. J. Mol. Biol. 300, 779–789.

Fotiadis, D., Scheuring, S., Müller, S., Engel, A., Müller, D.J., 2002. Controlled nanomanipulation of biological specimens with the atomic force microscope. Micron 33, 385–397.

Gorin, M.B., Yancey, S.B., Cline, J., Revel, J.P., Horwitz, J., 1984. The major intrinsic protein (MIP) of the bovine lens fiber membrane: characterization and structure based on cDNA cloning. Cell 39, 49–59.

Grigorieff, N., Ceska, T.A., Downing, K.H., Baldwin, J.M., Henderson, R., 1996. Electron-crystallographic refinement of the structure of bacteriorhodopsin. J. Mol. Biol. 259, 393–421.

Groth, G., Walker, J.E., 1997. Model of the *c*-subunit oligomer in the membrane domain of F-ATPases. FEBS Lett. 410, 117–123.

Hafner, J.H., Cheung, C.L., Woolley, A.T., Lieber, C.M., 2001. Structural and functional imaging with carbon nanotube AFM probes. Prog. Biophys. Mol. Biol. 77, 73–110.

Han, W., Lindsay, S.M., Jing, T., 1996. A magnetically driven oscillating microscope for operation in liquids. Appl. Phys. Lett. 69, 4111–4113.

Hand, G.M., Müller, D.J., Nicholson, B., Engel, A., Sosinsky, G.E., 2001. Isolation and characterization of gap junctions from tissue culture cells. J. Mol. Biol. 315, 587–600.

Hansma, H.G., Vesenka, J., Siegerist, C., Kelderman, G., Morrett, H., Sinsheimer, R.L., Elings, V., Bustamate, C., Hansma, P.K., 1992. Reproducible imaging and dissection of plasmid DNA under liquid with the atomic force microscope. Science 256, 1180–1184.

Hansma, P.K., Cleveland, J.P., Radmacher, M., Walters, D.A., Hillner, P.E., Bezanilla, M., Fritz, M., Vie, D., Hansma, H.G., Prater, C.B., Massie, J., Fukunaga, L., Gurley, J., Elings, V., 1994a. Tapping mode atomic force microscopy in liquids. Appl. Phys. Lett. 64, 1738–1740.

Hansma, P.K., Drake, B., Grigg, D., Prater, C.B., Yashar, F., Gurley, G., Elings, V., Feinstein, S., Lal, R., 1994b. A new, optical-lever based atomic force microscope. J. Appl. Phys. 76, 796–799.

Hargrave, P.A., 1991. Seven-helix receptors. Curr. Opin. Struct. Biol. 1, 575–581.

Hasler, L., Heymann, J.B., Engel, A., Kistler, J., Walz, T., 1998a. 2D crystallization of membrane proteins: rationales and examples. J. Struct. Biol. 121, 162–171.

Hasler, L., Walz, T., Tittmann, P., Gross, H., Kistler, J., Engel, A., 1998b. Purified lens major intrinsic protein (MIP) forms highly ordered tetragonal two-dimensional arrays by reconstitution. J. Mol. Biol. 279, 855–864.

Haupts, U., Tittor, J., Oesterhelt, D., 1999. Closing in on bacteriorhodopsin: progress in understanding the molecule. Annu. Rev. Biophys. Biomol. Struct. 28, 367–399.

Heinz, W.F., Hoh, J.H., 1999. Relative surface charge density mapping with the atomic force microscope. Biophys. J. 76, 528–538.

Heinzelmann, H., Pohl, D.W., 1994. Scanning near-field optical microscopy. Appl. Phys. A Solid Surf. 59, 89–101.

Helmreich, E.J.M., Hofmann, K.-P., 1996. Structure and function of proteins in G-protein coupled signal transfer. Biochem. Biophys. Acta 1286, 285–322.

Henderson, E., 1992. Imaging and nanodissection of individual supercoiled plasmids by atomic force microscopy. Nucleic Acids Res. 20, 445–447.

Henderson, R., Shertler, F.R.S., Shertler, G.F.X., 1990. The structure of bacteriorhodopsin and its relevance to the visual opsins and other seven-helix G-protein coupled receptors. Phil. Trans. R. Soc. London B 326, 379–389.

Heymann, J.B., Engel, A., 1999. Aquaporins: phylogeny, structure, and physiology of water channels. News Physiol. Sci. 14, 187–193.

Heymann, J.B., Engel, A., 2000. Structural clues in the sequences of the aquaporins. J. Mol. Biol. 295, 1039–1053.

Heymann, J.B., Müller, D.J., Landau, E., Rosenbusch, J., Pebay-Peroulla, E., Büldt, G., Engel, A., 1999. Charting the surfaces of purple membrane. J. Struct. Biol. 128, 243–249.

Heymann, J.B., Pfeiffer, M., Hildebrandt, V., Fotiadis, D., de Groot, B., Kabak, R., Engel, A., Oesterhelt, D., Müller, D.J., 2000. Conformations of the rhodopsin third cytoplasmic loop grafted onto bacteriorhodopsin. Structure 8, 643–644.

Hille, B., 1992. Ionic Channels of Excitable Membranes. Sinauer associates Inc., Sunderland, MA.

Hoh, J.H., Lal, R., John, S.A., Revel, J.-P., Arnsdorf, M.F., 1991. Atomic force microscopy and dissection of gap junctions. Science 253, 1405–1408.

Hoh, J.H., Sosinsky, G.E., Revel, J.-P., Hansma, P.K., 1993. Structure of the extracellular surface of the gap junction by atomic force microscopy. Biophys. J. 65, 149–163.

Howard, J., 2001. Mechanics of motor proteins and the cytoskeleton. Sinauer Associates Inc., Sunderland, MA.

Humphris, A.D.L., Tamayo, J., Miles, M.J., 2001. Active quality factor control in liquids for force spectroscopy. Langmuir 16, 7891–7894.

Israelachvili, J., 1991. Intermolecular & Surface Forces. Academic Press Limited, London.

Iwamoto, H., Czajkowsky, D.M., Cover, T.L., Szabo, G., Shao, Z., 1999. VacA from *Helicobacter pylori*: a hexameric chloride channel. FEBS Lett. 450, 101–104.

Jones, P.C., Fillingame, R.H., 1998. Genetic fusions of subunit c in the F_0 sector of H + -transporting ATP synthase. Functional dimers and trimers and determination of stoichiometry by cross-linking analysis. J. Biol. Chem. 273, 29701–29705.

Kamermans, M., Fahrenfort, I., Schultz, K., Janssen-Bienhold, U., Sjoerdsma, T., Weiler, R., 2001. Hemichannel-mediated inhibition in the outer retina. Science 292, 1178–1180.

Kimura, Y., Vassylev, D.G., Miyazawa, A., Kidera, A., Matsushima, M., Mitsuoka, K., Murata, K., Hirai, T., Fujiyoshi, Y., 1997. Surface of bacteriorhodopsin revealed by high-resolution electron microscopy. Nature 389, 206–211.

Klebba, P.E., Newton, S.M., 1998. Mechanisms of solute transport through outer membrane porins: burning down the house. Curr. Opin. Microbiol. 1, 238–247.

Kolbe, M., Besir, H., Essen, L.O., Oesterhelt, D., 2000. Structure of the light-driven chloride pump halorhodopsin at 1.8 A resolution. Science 288, 1390–1396.

Kourie, J.I., Wood, H.B., 2000. Biophysical and molecular properties of annexin-formed channels. Prog. Biophys. Mol. Biol. 73, 91–134.

Kunji, E.R., von Gronau, S., Oesterhelt, D., Henderson, R., 2000. The three-dimensional structure of halorhodopsin to 5 A by electron crystallography: a new unbending procedure for two-dimensional crystals by using a global reference structure. Proc. Natl. Acad. Sci. USA 97, 4637–4642.

Lakey, J.H., 1987. Voltage gating in porin channels. FEBS Lett. 211, 1–4.

Le Dain, A.C., Häse, C.C., Tommassen, J., Martinac, B., 1996. Porins of *E. coli*: unidirectional gating by pressure. EMBO J. 15, 3524–3528.

Lewis, A., Radko, A., Ben Ami, N., Palanker, D., Lieberman, K., 1999. Near-field scanning optical microscopy in cell biology. Trends Cell Biol. 9, 70–73.

Li, H., Liu, T.-F., Lazrak, A., Peracchia, C., Goldberg, G.S., Lampe, P.D., Johnson, R.G., 1996. Properties and regulation of gap junctional hemichannels in the plasma membrane of cultured cells. J. Cell Biol. 134, 1019–1030.

Lilie, H., Buchner, J., 1995. Interaction of GroEL with a highly structured folding intermediate: iterative binding cycles do not involve unfolding. Proc. Natl. Acad. Sci. USA 92, 8100–8104.

Luecke, H., Richter, H.-T., Lanyi, J.K., 1998. Proton transfer pathways in bacteriorhodopsin at 2.3 Angstrom resolution. Science 280, 1934–1937.

Luecke, H., Schobert, B., Richter, H.T., Cartailler, J.P., Lanyi, J.K., 1999. Structure of bacteriorhodopsin at 1.55 A resolution. J. Mol. Biol. 291, 899–911.

Manne, S., Gaub, H.E., 1995. Molecular organization of surfactants at solid–liquid interfaces. Science 270, 1480–1482.

Meixner, A.J., Kneppe, H., 1998. Scanning near-field optical microscopy in cell biology and microbiology. Cell Mol. Biol. (Noisy-le-grand) 44, 673–688.

Merritt, E.A., Kuhn, P., Sarfaty, S., Erbe, J.L., Holmes, R.K., Hol, W.G., 1998. The 1.25 A resolution refinement of the cholera toxin B-pentamer: evidence of peptide backbone strain at the receptor-binding site. J. Mol. Biol. 282, 1043–1059.

Michel, H., Oesterhelt, D., Henderson, R., 1980. Orthorhombic two-dimensional crystal form of purple membrane. Proc. Natl. Acad. Sci. USA 77, 338–342.

Mitsuoka, K., Hirai, T., Murata, K., Miyazawa, A., Kidera, A., Kimura, Y., Fujiyoshi, Y., 1999. The structure of bacteriorhodopsin at 3.0 Å resolution based on electron crystallography: implication of the charge distribution. J. Mol. Biol. 286, 861–882.

Möller, C., Allen, M., Elings, V., Engel, A., Müller, D.J., 1999. Tapping mode atomic force microscopy produces faithful high-resolution images of protein surfaces. Biophys. J. 77, 1050–1058.

Möller, C., Büldt, G., Dencher, N., Engel, A., Müller, D.J., 2000. Reversible loss of crystallinity on photobleaching purple membrane in presence of hydroxylamine. J. Mol. Biol. 301, 869–879.

Mou, J.X., Yang, J., Shao, Z.F., 1995. Atomic force microscopy of cholera toxin B-oligomers bound to bilayers of biologically relevant lipids. J. Mol. Biol. 248, 507–512.

Mou, J., Czajkowsky, D.M., Sheng, S., Ho, R., Shao, Z., 1996a. High resolution surface structure of *E. coli* GroES oligomer by atomic force microscopy. FEBS Lett. 381, 161–164.

Mou, J., Sheng, S., Ho, R., Shao, Z., 1996b. Chaperonins GroEL and GroES: views from atomic fore microscopy. Biophys. J. 71, 2213–2221.

Müller, D.J., Engel, A., 1997. The height of biomolecules measured with the atomic force microscope depends on electrostatic interactions. Biophys. J. 73, 1633–1644.

Müller, D.J., Engel, A., 1999. PH and voltage induced structural changes of porin OmpF explain channel closure. J. Mol. Biol. 285, 1347–1351.

Müller, D.J., Büldt, G., Engel, A., 1995. Force-induced conformational change of bacteriorhodopsin. J. Mol. Biol. 249, 239–243.

Müller, D.J., Baumeister, W., Engel, A., 1996a. Conformational change of the hexagonally packed intermediate layer of *Deinococcus radiodurans* imaged by atomic force microscopy. J. Bacteriol. 178, 3025–3030.

Müller, D.J., Schoenenberger, C.A., Büldt, G., Engel, A., 1996b. Immuno-atomic force microscopy of purple membrane. Biophys. J. 70, 1796–1802.

Müller, D.J., Amrein, M., Engel, A., 1997a. Adsorption of biological molecules to a solid support for scanning probe microscopy. J. Struct. Biol. 119, 172–188.

Müller, D.J., Engel, A., Carrascosa, J., Veléz, M., 1997b. The bacteriophage ø29 head-tail connector imaged at high resolution with atomic force microscopy in buffer solution. EMBO J. 16, 101–107.

Müller, D.J., Fotiadis, D., Scheuring, S., Müller, S.A., Engel, A., 1999a. Electrostatically balanced subnanometer imaging of biological specimens by atomic force microscopy. Biophys. J. 76, 1101–1111.

Müller, D.J., Sass, H.-J., Müller, S., Büldt, G., Engel, A., 1999b. Surface structures of native bacteriorhodopsin depend on the molecular packing arrangement in the membrane. J. Mol. Biol. 285, 1903–1909.

Müller, D.J., Dencher, N.A., Meier, T., Dimroth, P., Suda, K., Stahlberg, H., Engel, A., Seelert, H., Matthey, U., 2001a. ATP synthase: constrained stoichiometry of the transmembrane rotor. FEBS Lett. 504, 219–222.

Müller, D.J., Hand, G.M., Engel, A., Sosinsky, G., 2001b. Conformational changes in surface structures of isolated Connexin26 gap junctions observed by atomic force microscopy EMBO J. In press.

Müller, D.J., Kessler, M., Oesterhelt, F., Moeller, C., Oesterhelt, D., Gaub, H., 2002. Stability of bacteriorhodopsin α-helices and loops analyzed by single molecule force spectroscopy, submitted for publication.

Nikaido, H., 1989. Antimicrob. Agents Chemother. 33, 1831–1836.

Nikaido, H., Saier, M.H., 1992. Transport proteins in bacteria: common themes in their design. Science 258, 936–942.

Nikaido, H., Vaara, M., 1985. Molecular basis of bacterial outer membrane permeability. Microbiol. Rev. 49, 1–32.

Oesterhelt, D., 1998. The structure and mechanism of the family of retinal proteins from halophilic archaea. Curr. Opin. Struct. Biol. 8, 489–500.

Oesterhelt, D., Schuhmann, L., Gruber, H., 1974. Light-dependent reaction of bacteriorhodopsin with hydroxylamine in cell suspensions of *Halobacterium halobium*: demonstration of an apo-membrane. FEBS Lett. 44, 257–261.

Oesterhelt, F., Oesterhelt, D., Pfeiffer, M., Engel, A., Gaub, H.E., Müller, D.J., 2000. Unfolding pathways of individual bacteriorhodopsins. Science 288, 143–146.

Pebay-Peyroula, E., Rummel, G., Rosenbusch, J.P., Landau, E.M., 1997. X-ray structure of bacteriorhodopsin at 2.5 angstroms from microcrystals grown in lipidic cubic phases. Science 277, 1676–1681.

Persike, N., Pfeiffer, M., Guckenberger, R., Radmacher, M., Fritz, M., 2001. Direct observation of different surface structures on high-resolution images of native halorhodopsin. J. Mol. Biol. 310, 773–780.

Peters, J., Peters, M., Lottspeich, F., Schäfer, W., Baumeister, W., 1987. Nucleotide sequence of the gene encoding the *Deinococcus radiodurans* surface protein, derived amino acid sequence, and complementary protein chemical studies. J. Bacteriol. 169, 5216–5223.

Pfahnl, A., Dahl, G., 1999. Gating of cx46 gap junction hemichannels by calcium and voltage. Pflugers Arch. 437, 345–353.

Pfeiffer, M., Rink, T., Gerwert, K., Oesterhelt, D., Steinhoff, H.-J., 1999. Site-directed spin-labelling reveals the orientation of the amino acid side-chains in the E–F loop of bacteriorhodopsin. J. Mol. Biol. 287, 163–171.

Philippsen, A., Im, W., Engel, A., Schirmer, T., Roux, B., Müller, D.J., 2002. Imaging the electrostatic potential of transmembrane channels: atomic probe microscopy on OmpF porin. Biophys. J. 82, 1667–1676.

Pohl, P., Saparov, S.M., Borgnia, M.J., Agre, P., 2001. Highly selective water channel activity measured by voltage clamp: analysis of planar lipid bilayers reconstituted with purified Aqpz. Proc. Natl. Acad. Sci. USA 98, 9624–9629.

Putman, C.A.J., van der Werft, K., de Grooth, B.G., van Hulst, N.F., Greve, J., Hansma, P.K., 1992. A new imaging mode in the atomic force microscopy based on the error signal. SPIE 1639, 198–204.

Putman, C.A.J., Vanderwerf, K.O., Degrooth, B.G., Vanhulst, N.F., Greve, J., 1994. Tapping mode atomic force microscopy in liquid. Appl. Phys. Lett. 64, 2454–2456.

Rachel, R., Jakubowski, U., Tietz, H., Hegerl, R., Baumeister, W., 1986. Projected structure of the surface protein of *Deinococcus radiodurans* determined to 8 Å resolution by cryomicroscopy. Ultramicroscopy 20, 305–316.

Rastogi, V.K., Girvin, M.E., 1999. Structural changes linked to proton translocation by subunit c of the ATP synthase. Nature 402, 263–268.

Reviakine, I., Bergsma-Schutter, W., Brisson, A., 1998. Growth of protein 2-D crystals on supported planar lipid bilayers imaged in situ by AFM. J. Struct. Biol. 121, 356–361.

Reviakine, I., Bergsma-Schutter, W., Mazeres-Dubut, C., Govorukhina, N., Brisson, A., 2000. Surface topography of the p3 and p6 annexin V crystal forms determined by atomic force microscopy. J. Struct. Biol. 131, 234–239.

Rief, M., Gautel, M., Oesterhelt, F., Fernandez, J.M., Gaub, H.E., 1997. Reversible unfolding of individual titin immunoglobulin domains by AFM. Science 276, 1109–1112.

Rief, M., Gautel, M., Gaub, H.E., 2000. Unfolding forces of titin and fibronectin domains directly measured by AFM. Adv. Exp. Med. Biol. 481, 129–136.

Rotsch, C., Radmacher, M., 1997. Mapping local electrostatic forces with the atomic force microscope. Langmuir 13, 2825–2832.

Saint, N., Lou, K.L., Widmer, C., Luckey, M., Schirmer, T., Rosenbusch, J.P., 1996. Structural and functional characterization of OmpF porin mutants selected for larger pore size. J. Biol. Chem. 271, 20676–20680.

Saparov, S.M., Kozono, D., Rothe, U., Agre, P., Pohl, P., 2001. Water and ion permeation of aquaporin-1 in planar lipid bilayers. Major differences in structural determinants and stoichiometry. J. Biol. Chem. 276, 31515–31520.

Scheuring, S., Müller, D.J., Ringler, P., Heymann, J.B., Engel, A., 1999a. Imaging streptavidin 2D crystals on biotinylated lipid monolayers at high resolution with the atomic force microscopy. J. Microsc. 193, 28–35.

Scheuring, S., Ringler, P., Borgina, M., Stahlberg, H., Müller, D.J., Agre, P., Engel, A., 1999b. High resolution topographs of the *E. coli* waterchannel aquaporin Z.. EMBO J. 18, 4981–4987.

Scheuring, S., Reiss-Husson, F., Engel, A., Rigaud, J.L., Ranck, J.L., 2001. High-resolution AFM topographs of *Rubrivivax gelatinosus* light-harvesting complex LH2. EMBO J. 20, 3029–3035.

Schindler, H., Rosenbusch, J.P., 1978. Matrix protein from *E. coli* outer membranes forms voltage-controlled channels in lipid bilayers. Proc. Natl. Acad. Sci. USA 75, 3751–3755.

Schindler, H., Rosenbusch, J.P., 1981. Matrix protein in planar membranes: clusters of channels in a native environment and their functional assembly. Proc. Natl. Acad. Sci. USA 78, 2302–2306.

Schirmer, T., 1998. General and specific porins from bacterial outer membranes. J. Struct. Biol. 121, 101–109.

Schirmer, T., Phale, P.S., 1999. Brownian dynamics simulation of ion flow through porin channels. J. Mol. Biol. 294, 1159–1167.

Schmitt, L., Ludwig, M., Gaub, H.E., Tampe, R., 2000. A metal-chelating microscopy tip as a new toolbox for single-molecule experiments by atomic force microscopy. Biophys. J. 78, 3275–3285.

Seelert, H., Poetsch, A., Dencher, N.A., Engel, A., Stahlberg, H., Müller, D.J., 2000. Proton powered turbine of a plant motor. Nature 405, 418–419.

Selvin, P.R., 2000. The renaissance of fluorescence resonance energy transfer. Nat. Struct. Biol. 7, 730–734.

Simpson, A.A., Tao, Y., Leiman, P.G., Badasso, M.O., He, Y., Jardine, P.J., Olson, N.H., Morais, M.C., Grimes, S., Anderson, D.L., Baker, T.S., Rossmann, M.G., 2000. Structure of the bacteriophage phi29 DNA packaging motor. Nature 408, 745–750.

Sleytr, U.B., 1997. Basic and applied S-layer research: an overview. FEMS Microbiol. Rev. 20, 5–12.

Sleytr, U.B., Messner, P., Pum, D., Sára, M., 1993. Crystalline bacterial cell surface layers: general principles and application potential. J. Appl. Bacteriol. Symp. Suppl. 74, 21S–32S.

Song, L., Hobaugh, M.R., Shustak, C., Cheley, S., Bayley, H., Gouaux, J.E., 1996. Structure of staphylococcal alpha-hemolysin, a heptameric transmembrane pore. Science 274, 1859–1866.

Stahlberg, H., Müller, D.J., Suda, K., Fotiadis, D., Engel, A., Matthey, U., Meier, T., Dimroth, P., 2001. Bacterial ATP synthase has an undecameric rotor. EMBO Rep. 21, 1–5.

Stock, D., Leslie, A.G., Walker, J.E., 1999. Molecular architecture of the rotary motor in ATP synthase. Science 286, 1700–1705.

Stock, D., Gibbons, C., Arechaga, I., Leslie, A.G., Walker, J.E., 2000. The rotary mechanism of ATP synthase. Curr. Opin. Struct. Biol. 10, 672–679.

Tamayo, J., Humphris, A.D.L., Miles, M.J., 2000. Piconewton regime dynamic force microscopy in liquid. Appl. Phys. Lett. 77, 582–584.

Todt, J.C., Rocque, W.J., McGroarty, E.J., 1992. Effects of pH on bacterial porin function. Biochemistry 31, 10471–10478.

van Huizen, R., Czajkowsky, D.M., Shi, D., Shao, Z., Li, M., 1999. Images of oligomeric Kv beta 2, a modulatory subunit of potassium channels. FEBS Lett. 457, 107–111.

Varadaraj, K., Kushmerick, C., Baldo, G.J., Bassnett, S., Shiels, A., Mathias, R.T., 1999. The role of MIP in lens fiber cell membrane transport. J. Membr. Biol. 170, 191–203.

Vesenka, J., Guthold, M., Tang, C.L., Keller, D., Delaine, E., Bustamante, C., 1992. Substrate preparation for reliable imaging of DNA molecules with the scanning force microscope. Ultramicroscopy 42–44, 1243–1249.

Viani, M.B., Schäfer, T.E., Chand, A., Rief, M., Gaub, H., Hansma, P.K., 1999. Small cantilevers for force spectroscopy of single molecules. J. Appl. Phys. 86, 2258–2262.

Viani, M.B., Pietrasanta, L.I., Thompson, J.B., Chand, A., Gebeshuber, I.C., Kindt, J.H., Richter, M., Hansma, H.G., Hansma, P.K., 2000. Probing protein–protein interactions in real time. Nat. Struct. Biol. 7, 644–647.

Vie, V., van Man, N., Pomarede, P., Dance, C., Schwartz, J.L., Laprade, R., Frutos, A., Rang, C., Masson, L., Heitz, F., Le Grimellec, C., 2001. Lipid induced formation of the Bacillus thuringiensis CrylAa insecticidal toxin. J. Membr. Biol. 180, 195–203.

Vinckier, A., Gervasoni, P., Zaugg, F., Ziegler, U., Lindner, P., Groscurth, P., Pluckthun, A., Semenza, G., 1998. Atomic force microscopy detects changes in the interaction forces between GroEL and substrate proteins. Biophys. J. 74, 3256–3263.

Walz, T., Typke, D., Smith, B.L., Agre, P., Engel, A., 1995. Projection map of aquaporin-1 determined by electron crystallography. Nat. Struct. Biol. 2, 730–732.

Walz, T., Tittmann, P., Fuchs, K.H., Müller, D.J., Smith, B.L., Agre, P., Gross, H., Engel, A., 1996. Surface topographies at subnanometer-resolution reveal asymmetry and sidedness of aquaporin-1. J. Mol. Biol. 264, 907–918.

Weiss, S., 1999. Fluorescence spectroscopy of single biomolecules. Science 283, 1676–1683.

Weiss, S., 2000. Measuring conformational dynamics of biomolecules by single molecule fluorescence spectroscopy. Nat. Struct. Biol. 7, 724–729.

Weiss, M.S., Abele, U., Weckesser, J., Welte, W., Schlitz, E., Schulz, G.E., 1991. Molecular architecture and electrostatic properties of a bacterial porin. Science 254, 1627–1630.

Wilkens, S., Capaldi, R.A., 1998. Electron microscopic evidence of two stalks linking the F_1 and F_0 parts of the *E. coli* ATP synthase. Biochim. Biophys. Acta 1365, 93–97.

Yang, J., Tamm, L.K., Tillack, T.W., Shao, Z., 1993. New approach for atomic force microscopy of membrane proteins. J. Mol. Biol. 229, 286–290.